

Peptide programming of supramolecular vinylidene fluoride ferroelectric phases

<https://doi.org/10.1038/s41586-024-08041-4>

Yang Yang¹, Hiroaki Sai^{1,2}, Simon A. Egner², Ruomeng Qiu³, Liam C. Palmer^{1,3} & Samuel I. Stupp^{1,2,3,4,5,6}✉

Received: 20 November 2023

Accepted: 12 September 2024

Published online: 9 October 2024

 Check for updates

Ferroelectric structures have spontaneous macroscopic polarization that can be inverted using external electric fields and have potential applications including information storage, energy transduction, ultralow-power nanoelectronics^{1,2} and biomedical devices³. These functions would benefit from nanoscale control of ferroelectric structure, the ability to switch polarization with lower applied fields (low coercive field) and biocompatibility. Soft ferroelectrics based on poly(vinylidene fluoride) (PVDF)^{4–6} have a thermodynamically unstable ferroelectric phase in the homopolymer, complex semi-crystalline structures, and high coercive fields. Here we report on ferroelectric materials formed by water-soluble molecules containing only six VDF repeating units covalently conjugated to a tetrapeptide, with the propensity to assemble into the β-sheet structures that are ubiquitous in proteins. This led to the discovery of ribbon-shaped ferroelectric supramolecular assemblies that are thermodynamically stable with their long axes parallel to both the preferred hydrogen-bonding direction of β-sheets and the bistable polar axes of VDF hexamers. Relative to a commonly used ferroelectric copolymer, the biomolecular assemblies exhibit a coercive field that is two orders of magnitude lower, as the result of supramolecular dynamics, and a similar level of remnant polarization, despite having a peptide content of 49 wt%. Furthermore, the Curie temperature of the assemblies is about 40 °C higher than that of a copolymer containing a similar amount of VDF. This supramolecular system was created using a biologically inspired strategy that is attractive in terms of sustainability and that could lead to new functions for soft ferroelectrics.

The field of ferroelectrics has largely been dominated by hard inorganic materials, which often contain toxic or rare metals, such as lead or niobium, respectively. Organic ferroelectrics are generating great interest because of their lightness, mechanical flexibility, low toxicity and potential for use as structures that interface biological systems⁷ or integrate well into soft electronics^{8,9}. Previously studied organic ferroelectrics based on small molecules include co-crystals in which hydrogen bonding^{10–12} and charge transfer¹³ help to create the non-centrosymmetric structures required for spontaneous polarization. However, VDF-based fluoropolymers have been the most technologically important organic ferroelectrics for decades, and they are still the only soft ferroelectric that has been successfully used in many applications^{6,14}.

Ferroelectricity in crystalline PVDF arises from the all-*trans* conformation of the backbone, which contains strong CF₂ dipoles in alternate carbon atoms, forming the so-called β-phase¹⁵. The β-phase is unique among organic ferroelectrics in that it generates multiaxial ferroelectricity in the cross-section of the backbone¹⁶, a feature that is required to achieve good ferroelectric performance for thin-film applications and is a challenge in small-molecule ferroelectrics^{17,18}. A major limitation of

PVDF, however, is the fact that the β-phase is not thermodynamically stable relative to its non-polar crystal structures. Accessing the β-phase therefore requires either mechanical stretching of the polymer or random copolymerization with trifluoroethylene (TrFE) structural units, which do not contribute directly to ferroelectricity¹⁵. Furthermore, the high coercive field (around 500 kV cm⁻¹) of PVDF-based polymers, which is partly due to the high macromolecular-torsion energy barrier¹⁹, has hindered their application in low-voltage memory and other low-power electronics⁶. Previous studies have shown that β-phase crystallization is favoured in oligomeric vinylidene fluoride with a degree of polymerization of less than 10, but ferroelectric behaviour was not reported²⁰. Also, highly crystalline β-phase with in-plane chain orientation could be formed in longer oligomers by using vapour deposition, but only at cryogenic temperatures (lower than -50 °C)²¹, which led to coercive fields that were even higher (more than 1,000 kV cm⁻¹) than those observed in PVDF-based polymers²². Given the emerging opportunities in organic ferroelectrics, one important scientific goal is to develop new approaches to create preferential organizations of these functional structures at nanoscale sizes. Previous studies have

¹Simpson Querrey Institute for BioNanotechnology, Northwestern University, Chicago, IL, USA. ²Department of Materials Science and Engineering, Northwestern University, Evanston, IL, USA.

³Department of Chemistry, Northwestern University, Evanston, IL, USA. ⁴Department of Biomedical Engineering, Northwestern University, Evanston, IL, USA. ⁵Department of Medicine, Northwestern University, Chicago, IL, USA. ⁶Center for Bio-inspired Energy Science, Northwestern University, Evanston, IL, USA. ✉e-mail: s-stupp@northwestern.edu

grafted VDF oligomers to synthetic aromatic cores²³, but there has been no supramolecular programming of a thermodynamically stable ferroelectric phase. Here we report on supramolecular programming by short peptide sequences to direct the organization of VDF oligomers (OVDF) into a thermodynamically stable ferroelectric phase. To achieve this, we used molecules known as peptide amphiphiles (PAs), in which peptides are conjugated to hydrophobic segments to drive assembly into one-dimensional nanostructures in water^{24,25}.

Morphology and crystal structures

We selected the tetrapeptide Val-Glu-Val-Glu (VEVE) for the synthesis of an OVDF-PA that was previously known to form wide, nanoscale ribbon-like structures²⁶ that could generate large ferroelectric domains. To potentially create supramolecular nanostructures with different morphologies, we also synthesized the β -sheet-forming peptide sequences VVEE, VEVE and EVEV. The oligomers were synthesized with three to seven VDF repeat units (VDF₃ to VDF₇) and terminated with carboxylic acids (Supplementary Section 1). We also prepared the three PAs with non-fluorinated tails containing 16 carbon atoms as controls because these have a similar length (2.10 nm) to the VDF₆ tail (1.97 nm) in their extended conformation. After heating aqueous solutions of the OVDF-PAs to 80 °C and slowly cooling them to room temperature, they all formed well-defined supramolecular structures with lengths on the order of micrometres, except for **VDF₄-EVEV** and all the VDF₃-PAs, which mainly formed spherical micelles, as observed by liquid-state atomic force microscopy (AFM) (Supplementary Fig. 1). Transmission electron microscopy (TEM) indicates that the supramolecular structures of all the OVDF-PAs are retained in the dried state (Supplementary Fig. 2). Solution small-angle X-ray scattering (SAXS) patterns of the OVDF-PAs in the low-*q* region reveal slopes of approximately −2 (Supplementary Fig. 3), which is consistent with the ribbon-like structures observed by TEM and AFM. As shown in Fig. 1b, **VDF₆-VVEE** PA forms narrow ribbons with an average width of about 30 nm. By contrast, **VDF₆-VEVE** forms flat ribbons with widths of more than 100 nm (Fig. 1c and Supplementary Fig. 4). Interestingly, **VDF₆-EVEV** forms a highly twisted ribbon morphology with an average width of 30–50 nm and a pitch length of about 70 nm (Fig. 1d). We propose that the presence of a bulky and charged glutamic acid side chain near the interface with the hydrophobic core in EVEV, which plays an important role in the secondary structure of peptide assemblies^{27,28}, distorts the alignment of molecules, resulting in a twisted morphology. Height measurements using AFM indicate that **VDF₆-VVEE** assembles into ribbons 5.5 nm thick, indicating a bilayer structure with partial interdigitation of OVDF tails of approximately 1 nm (Fig. 1e). **VDF₆-VEVE** and **VDF₆-EVEV** form ribbons with a height of about 4.5 nm, indicating that the OVDF tails are fully interdigitated (Fig. 1f,g). The assemblies with VDF₄ and VDF₅ tails show similar packing to the corresponding VDF₆-PAs (Supplementary Fig. 5). Extending the OVDF tail length from VDF₆ to VDF₇ results in shorter assemblies that have widths of less than 75 nm and a flat morphology for all three peptide sequences (Supplementary Fig. 6), indicating that VDF₆-PAs nanostructures may support larger crystalline domains, so we then focused on the VDF₆-PAs.

Next we characterized the molecular packing of the OVDF tails in the supramolecular structures to compare them with those known in the covalent polymer PVDF. Fourier-transform infrared (FTIR) spectroscopy using attenuated total reflectance (ATR) of OVDF-PAs with tails longer than four VDF repeats revealed the presence of peaks characteristic of the electroactive β -phase at 1,275 cm^{−1} (CF₂ symmetric stretching) and 837 cm^{−1} (CH₂ rocking)²⁹, as well as the amide I band corresponding to β -sheet peptides of around 1,622–1,631 cm^{−1} (C=O stretching)³⁰ (Fig. 2a–c). The absorption peaks of the β -sheet become sharper and exhibit a redshift as the length of the OVDF tail increases, indicating stronger hydrogen bonding in the β -sheet structure³⁰. These results demonstrate that the β -sheet supramolecular structure

spontaneously promotes the crystallization of OVDF into the polar β -phase without either mechanical intervention or the presence of trifluoroethylene structural units. Interestingly, regardless of the length of the OVDF segment, the VEVE peptide sequence, which gives rise to flat nanostructures, is the only one that generates only the polar phase in the supramolecular assemblies. Mutation of this sequence to either VVEE or EVEV results in a small amount of the non-electroactive α -phase.

We then obtained X-ray scattering scans of the experimental systems in solution using synchrotron radiation. The wide-angle X-ray scattering (WAXS) patterns of the OVDF-PAs (Fig. 2d) and the analogous PAs with non-fluorinated tails (Supplementary Fig. 8) all show a peak corresponding to a d-spacing of 4.7 Å, which is consistent with the typical distance in biological and synthetic β -sheets. Furthermore, the middle-angle X-ray scattering (MAXS) region of **VDF₆-VEVE** and **VDF₆-VVEE** revealed the expected spacing of 8.8 Å between β -sheets, which is similar to values previously reported for PA assemblies^{26,31} and to the a axis spacing in the ferroelectric β -phase in PVDF (8.58 Å)³². By contrast, the EVEV system has a larger spacing between β -sheets of about 9.8 Å, which in turn better matches the b -axis spacing of the PVDF α -phase (9.64 Å) (Fig. 2d and Supplementary Fig. 9). Furthermore, the WAXS patterns shown in Fig. 2d exhibit peak broadening and an increasing amorphous halo as the peptide sequences change from VEVE to VVEE and EVEV. This trend is consistent with the intensities of the small shoulder observed between 1,647 and 1,660 cm^{−1} in FTIR spectra (Fig. 2e), which is assigned to the α -helix or disordered peptides³⁰, indicating an increasing level of internal disorder and supramolecular motion in these three different assemblies. As shown in Fig. 2f–h, selected area electron diffraction (SAED) and the azimuthally integrated patterns (Supplementary Fig. 10d) showed features similar to those observed in the WAXS scans, indicating that the crystal structures of the OVDF-PA assemblies are retained in the dried state (see Supplementary Table 1). These diffraction patterns reveal spacings in the supramolecular structure that are commensurate with those found in the electroactive crystalline domains of the PVDF polymer. This is illustrated by the top-view schematic representation of the peptide β -sheet and β -phase OVDF crystal structures in **VDF₆-VEVE** (Fig. 2i), thereby explaining, at least in part, the observed programming of the polar phase by the peptide segments.

Ferroelectricity of OVDF-PA assemblies

Dried-state thin films of the OVDF-PA assemblies were prepared by casting 20 mM annealed solutions on a SiO₂ substrate using photolithographically patterned platinum electrodes (Supplementary Fig. 11). The AFM images of the surface of the samples show randomly oriented nanoscale ribbons across the 2 μm gap between the electrodes (Supplementary Fig. 12). Dielectric spectra and leakage-current measurements of the samples showed a very low loss tangent (less than 0.1) over a wide frequency range (Supplementary Fig. 14) and a high resistance (more than 10¹¹ Ω) (Supplementary Fig. 15), respectively. These results indicate negligible dielectric loss of the samples, favouring high-performance ferroelectric behaviour. To verify ferroelectric behaviour in the supramolecular assemblies, we obtained polarization versus electric-field curves (P-E loops) of samples by subtracting the linear contributions from the resistive loss, P_{RL} , and polarization, P_{CL} , to isolate the nonlinear ferroelectric polarization (Supplementary Fig. 17 and Supplementary Table 2). Because the electric field generated by the in-plane electrodes is not uniform, the P-E loops presented here were plotted using the average electric field applied across the electrode gap. Calibration measurements on PVDF and the commonly used ferroelectric copolymer indicate that the observed coercive field should be multiplied by a coefficient of 1.53, and the polarization strengths measured on the in-plane electrodes are also calibrated (Methods). As shown in Fig. 3a, **VDF₆-VEVE** assemblies show typical ferroelectric hysteresis loops with a remnant polarization (P_r) close to saturation values

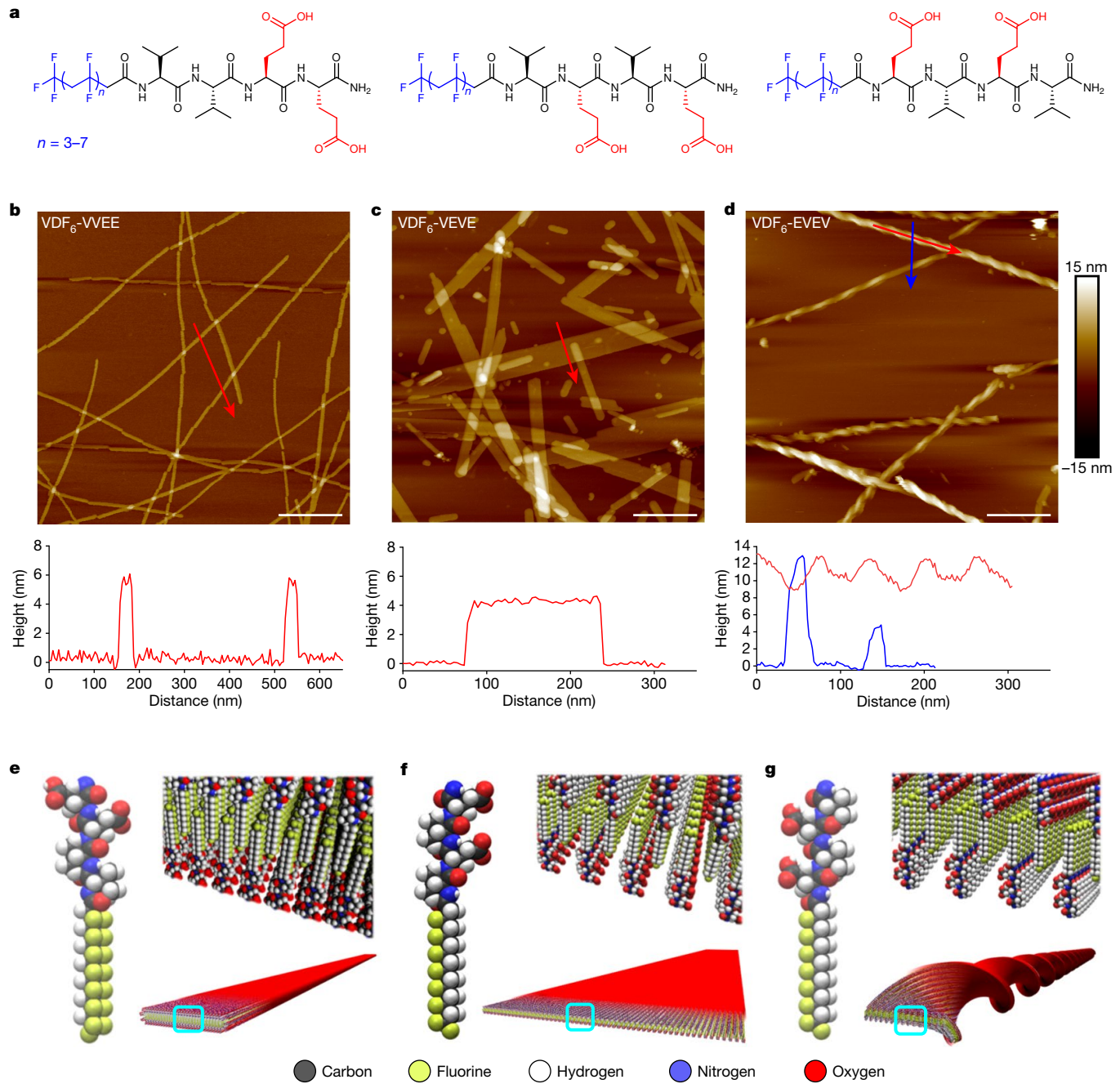


Fig. 1 | Molecular structures, morphologies and supramolecular architectures of the OVDF-PA assemblies. **a**, Chemical structures of the OVDF-PAs containing hydrophobic segments with 3–6 VDF repeat units and the peptide sequences VVEE, VEVE and EVEV (left to right). **b–d**, Liquid AFM images of $\text{VDF}_6\text{-VVEE}$ (**b**; scale bar, 400 nm), $\text{VDF}_6\text{-VEVE}$ (**c**; scale bar, 400 nm) and $\text{VDF}_6\text{-EVEV}$ (**d**; scale bar, 200 nm) cast from 20 mM aqueous solutions after annealing (corresponding height profiles were measured along the arrows shown). **e–g**, Molecular illustrations of supramolecular architectures in $\text{VDF}_6\text{-VVEE}$ (**e**), $\text{VDF}_6\text{-VEVE}$ (**f**) and $\text{VDF}_6\text{-EVEV}$ (**g**) assemblies.

$\text{VDF}_6\text{-EVEV}$ (**d**; scale bar, 200 nm) cast from 20 mM aqueous solutions after annealing (corresponding height profiles were measured along the arrows shown). **e–g**, Molecular illustrations of supramolecular architectures in $\text{VDF}_6\text{-VVEE}$ (**e**), $\text{VDF}_6\text{-VEVE}$ (**f**) and $\text{VDF}_6\text{-EVEV}$ (**g**) assemblies.

(the shorter OVDF tails result in the formation of narrower ribbons with a weaker ferroelectric response; Supplementary Fig. 25). In $\text{VDF}_6\text{-VVEE}$, ferroelectric hysteresis was also observed but with a lower coercive field (E_c) and a lower P_r than $\text{VDF}_6\text{-VEVE}$ (Fig. 3b). As expected for a system with an E_c much lower than the applied field, a saturation polarization (P_s) was observed beyond P_r for $\text{VDF}_6\text{-VVEE}$ (Fig. 3b). Interestingly, when the peptide sequence was inverted from VEVE to EVEV, we observed differently shaped P-E loops with low E_c and P_r values (Fig. 3c).

The much narrower P-E loops in the $\text{VDF}_6\text{-EVEV}$ samples are characteristic of the ferroelectric ‘relaxor’ phases³³. In these phases, the ferroelectric domains are small and weakly coupled with each other, as indicated by the low E_c , enabling efficient energy transduction, such as

strong electromechanical actuation. In PVDF, relaxor phases have previously been reported by introducing defects using electron irradiation³⁴ or the addition of bulky monomers^{4,35}, but precise control of VDF crystal domains on the nanoscale has not to our knowledge been reported. Here, the twisted morphology (Fig. 1c) of self-assembled peptide segments could be giving rise to the uncoupled small domains characteristic of a relaxor. In this relaxor system, the inverted peptide sequence has a low propensity to form β -sheets and, if shorter hydrophobic tails are used, one observes a lossy dielectric response (Supplementary Fig. 26) (symmetrical cigar-shaped loops³⁶ rather than ferroelectricity). P-E loops of VDF₇-PA assemblies exhibit low ferroelectric polarization (Supplementary Fig. 27), and FTIR of $\text{VDF}_7\text{-VEVE}$ assemblies shows a

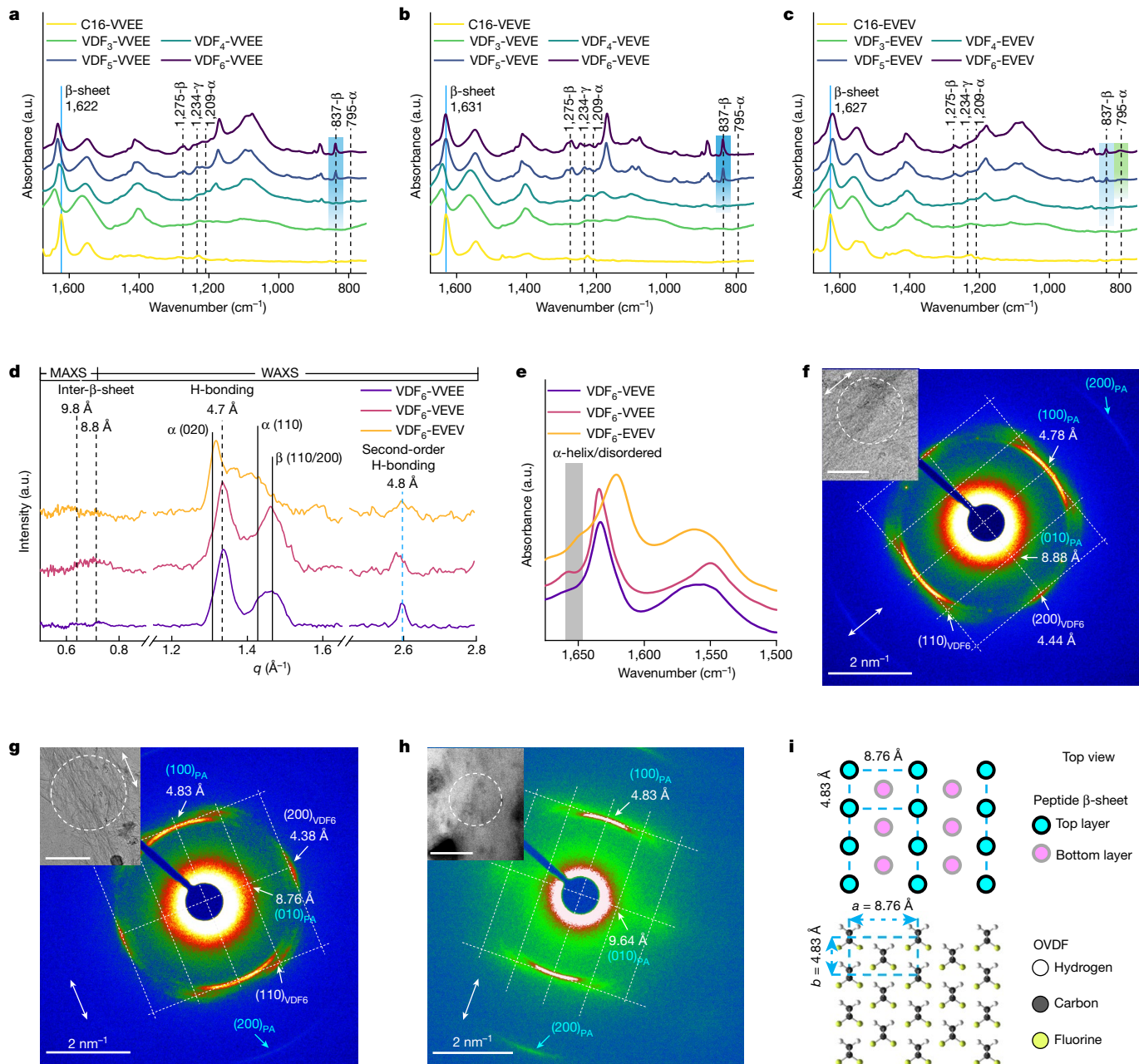


Fig. 2 | Crystal structures of the OVDF-PA assemblies. **a–c**, ATR-FTIR spectra of VVEE (**a**), VEVE (**b**) and EVEV (**c**) -PA assemblies dried from 10 mM annealed solution indicating peaks corresponding to amide I absorption in peptide β-sheets and peaks characteristic of the crystalline α, β and γ phases of vinylidene fluoride chains; a.u., absorbance units. **d**, X-ray scattering patterns of **VDF₆-VVVE**, **VDF₆-VEVE** and **VDF₆-EVEV** assemblies in solution for the MAXS and WAXS regions. Reflections of the inter-β-sheet spacing and hydrogen-bonding spacing are indicated by dashed black lines, and scattering from the α- and β-phases of vinylidene fluoride chain crystals are indicated by solid lines. **e**, FTIR spectra of VDF₆-PA assemblies in the peptide region. The small shoulder highlighted in grey between 1,647 cm⁻¹ and 1,660 cm⁻¹ is assigned to C=O stretching bands in the α-helix or disordered peptides (see text).

The intensities in **a–e** are offset vertically for clarity. **f–h**, SAED of **VDF₆-VVVE** (**f**; inset scale bar, 500 nm), **VDF₆-VEVE** (**g**; inset scale bar, 1 μm) and **VDF₆-EVEV** (**h**; inset scale bar, 1 μm) assemblies with indexing corresponding to hydrogen bonding in β-sheets and α- and β-phase OVDF. Insets show the corresponding electron micrographs of the supramolecular assemblies; the dashed white circles indicate the apertures of the selected areas (white double arrows in **f–h** indicate the long axes of the partly aligned **VDF₆-VVVE** and **VDF₆-VEVE** assemblies). **i**, Top-view schematic representation of peptide β-sheet and β-phase OVDF crystal structures in **VDF₆-VEVE**, showing the molecular spacing indexed in (**g**), in which $d[(010)_{PA}]$ matches $2d[(200)_{VDF6}]$ and $d[(100)_{PA}]$ matches $d[(010)_{VDF6}]$.

low content of β-phase OVDF (Supplementary Fig. 28). These observations indicate a weakened programming ability of the tetrapeptides for OVDF tails that are longer than VDF₆, which we attribute to their greater van der Waals forces becoming a dominant interaction in the system³⁷. To summarize the effect of peptide sequence and OVDF tail length on the properties of the 15 VDF_n-PA ($n = 3–7$) assemblies investigated, we

show in Supplementary Fig. 29 statistics for key parameters, including the width of the assemblies, the content of β- and α-phase OVDF, remnant polarization P_r , and P_r/P_s , which is equal to 1.0 for ideal ferroelectric behaviour. We have identified **VDF₆-VEVE** and **VDF₆-EVEV** as the optimal chemical structures for organization into ferroelectric and relaxor-like nanostructures, respectively.

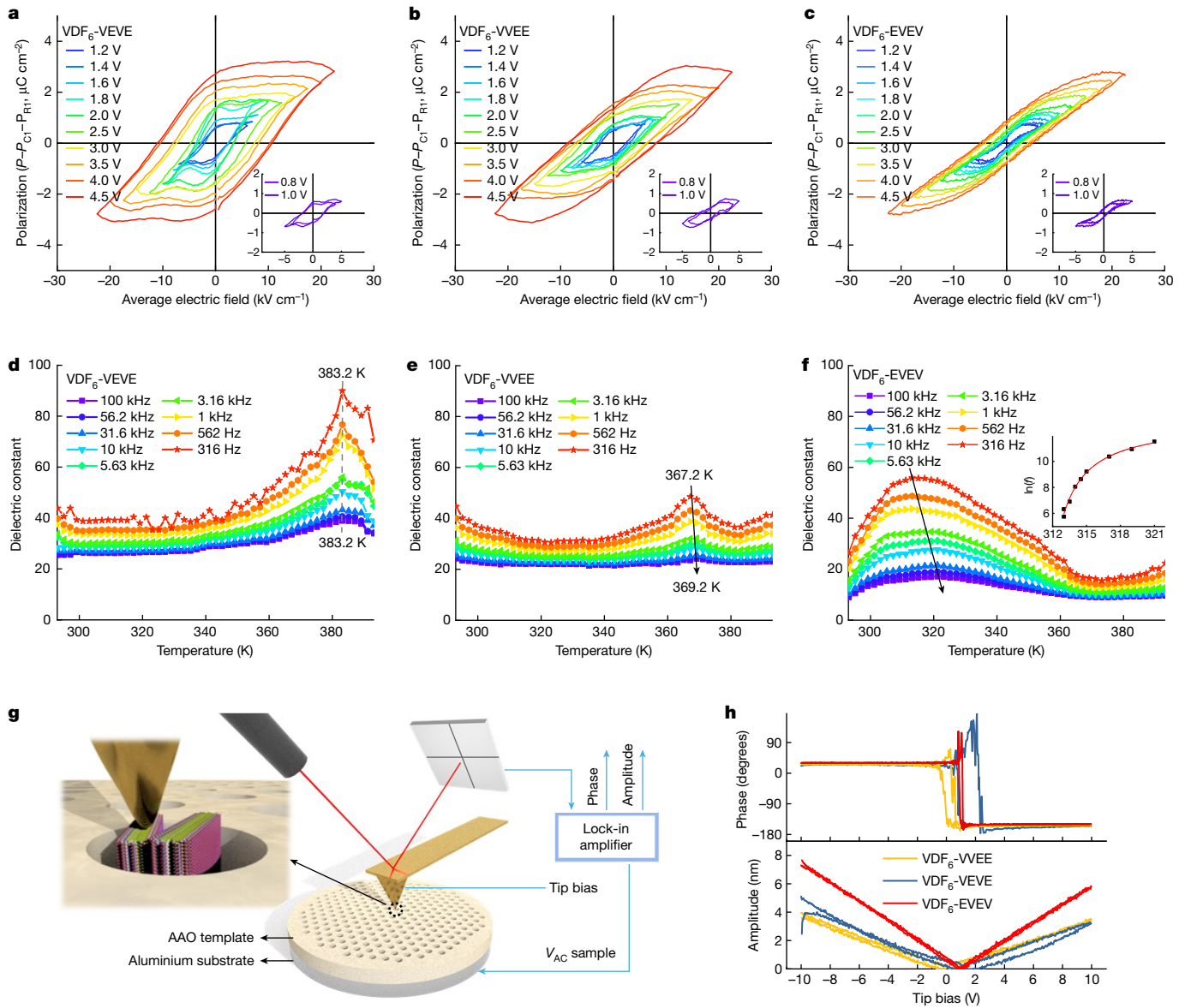


Fig. 3 | Ferroelectricity of OVDF-PA samples. **a–c**, Polarization versus electric field (P - E) loops of **VDF₆-VEVE** (a), **VDF₆-VVVE** (b) and **VDF₆-EVEV** (c). **d–f**, Variable-temperature dielectric constant for **VDF₆-VEVE** (d), **VDF₆-VVVE** (e) and **VDF₆-EVEV** (f)-PA thin films at different frequencies. Grey arrows show the dependence of the dielectric constant peak on the frequency of the applied

electric field when heated. The inset in f shows the fitting of the measured dielectric constant peaks using the Vogel–Fulcher law. **g**, Illustration of PFM butterfly loop measurements on PA samples prepared on porous AAO films with a conductive substrate; V_{AC} , the voltage of alternating-current signal. **h**, PFM amplitude and phase hysteresis loops for **VDF₆-PA** samples.

To verify the ferroelectric-to-paraelectric transition and the corresponding Curie temperature (T_C), the variable-temperature dielectric constant of PA thin films was measured at different frequencies. For the ferroelectric systems **VDF₆-VEVE** and **VDF₆-VVVE**, we observed narrow transition peaks that were independent of frequency, indicating Curie transition points T_C (Fig. 3d,e). The **VDF₆-VEVE** assemblies show the highest T_C at 110 °C, which is much higher than that of the ferroelectric copolymer containing about the same weight percent of VDF units (a T_C of around 66 °C for the copolymer containing 55 mol% VDF units)³⁸. As the OVDF tail length was shortened (Supplementary Fig. 31), a decreasing T_C was observed in the OVDF-VEVE and OVDF-VVVE samples, and we attribute this to the dependence of the ferroelectric-to-paraelectric transitions on domain size³³. P - E loops corresponding to **VDF₆-VEVE** and **VDF₆-VVVE** samples measured at high temperature showed lower remnant polarization and more lossy behaviour with heating to 80 °C, whereas **VDF₆-VEVE** exhibited stable ferroelectricity over a wide temperature range (Extended Data Fig. 1).

For the relaxor phase (**VDF₆-EVEV**), we observed, as expected³⁴, that the maximum in dielectric constant shifts to higher temperatures with increasing frequency (Fig. 3f). As shown in the inset of Fig. 3f, this frequency-dependent maximum in dielectric constant as a function of temperature can be modelled well using the Vogel–Fulcher law, which demonstrates relaxor behaviour:

$$\ln f = \ln f_0 - U / [k_B(T_m - T_f)] \quad (1)$$

where f is the frequency, f_0 is an empirical parameter called the attempt frequency that is generated by fitting, U is the activation energy, k_B is the Boltzmann constant, T_m is the temperature at the maximum in dielectric constant and T_f is the freezing temperature. Fitting our data to this equation yielded a T_f value of 37.2 °C, which is similar to those of other reported relaxor materials^{5,34} and supports robust relaxor-like properties in our system at around room temperature.

To investigate the electromechanical properties of the OVDF-PA nanostructures, we used piezoresponse force microscopy (PFM) on samples placed in the pores of anodic aluminium oxide (AAO) films (Methods) such that the electric field can be applied along the long axis of the PA ribbons (Fig. 3g). As shown in Fig. 3h and Supplementary Figs. 26–34, **VDF₆-VEVE** qualitatively exhibits typical piezoresponse hysteresis loops and the highest switching voltage, whereas **VDF₆-EVEV** shows negligible hysteresis (phase curve) along with the highest actuation amplitude. We interpret this observation to be the result of poor coupling among isolated small polar domains generated in twisted supramolecular assemblies.

Role of peptides in OVDF crystallization

We sought to determine the role of the peptide segments in the formation of the ferroelectric β -phase. For this purpose, we raised the pH of solutions of **VDF₆-VEVE** assemblies from pH 7 to pH 9 to ionize glutamic acid residues and increase the electrostatic repulsion in the assemblies. This resulted, as expected³¹, in a sizeable loss of β -sheet organization, and interestingly the ferroelectric domains disappeared (Fig. 4a). At pH 10, the β -sheet structure diminished further, and only the signature of non-ferroelectric α -phase OVDF was observed by FTIR (Fig. 4a). The β -phase OVDF and β -sheets could easily be recovered when the pH of the solution was returned to neutral (Fig. 4b). We also established that **VDF₆-COOH** cannot crystallize after being annealed in the dried state and does not give rise to ferroelectricity, only to typical lossy behaviour (Supplementary Figs. 38–42). Furthermore, we explored other peptides, including one with a shortened sequence (**VDF₆-VE**) and one in which we replaced valine (V) with isoleucine (I), which has a high β -sheet propensity (**VDF₆-IEIE**). These new molecules formed fibrous assemblies but exhibited low ferroelectricity, possibly owing to weak β -sheet formation in the case of **VDF₆-VE** and a lattice mismatch in **VDF₆-IEIE** (Supplementary Sections 5.2 and 5.3). We interpret these results as a strong indication of the thermodynamic stability of the all-*trans* conformation templated by β -sheets in supramolecular assemblies, which is not the case in pure PVDF.

Given the thermodynamically stable ferroelectric β -phase as a result of peptide programming, we attributed the observed high-temperature electroactive properties to the strong hydrogen-bonding interactions in β -sheets. Differential scanning calorimetry (DSC) on the annealed OVDF-PA solutions shows a single sharp exothermic peak (Fig. 4c–e), indicating that the OVDF regions and β -sheets synergistically order within a narrow temperature window. In the ferroelectric polymer PVDF, β -phase crystals formed by mechanical stretching are transformed into the thermodynamically stable but non-ferroelectric α -phase when the material has annealed near its melting point¹⁵. By contrast, VDF₆-PA supramolecular assemblies do not reveal the formation of the α -phase after being annealed slightly below, and even well above, their melting points (Supplementary Figs. 49 and 50). In the relaxor phase formed by **VDF₆-EVEV**, containing weak β -sheet structures, a decrease in the OVDF β -phase is observed after annealing at 120 °C (Supplementary Fig. 49).

Variable-temperature WAXS was performed using unannealed OVDF-PA solutions to investigate their melting and crystallization behaviour. Interestingly, **VDF₆-VEVE** shows a phase transition of the initial α -phase OVDF, which may be formed because of the kinetic traps before annealing, to the dominant β -phase after the heating–cooling cycle (Fig. 4f). For **VDF₆-VEVE**, the scattering peaks of the β -sheets disappear and the formation of α -phase OVDF was observed after heating to above its melting point followed by fast cooling (Supplementary Fig. 52). To determine the lattice orientation of β -phase OVDF crystals relative to the hydrogen-bonding direction in β -sheet structures, polarized FTIR was done with aligned VDF₆-PA nanofibres (Methods and Extended Data Fig. 2). The spectra indicate that the net dipole moment of the ferroelectric phase is aligned parallel to the long axis of the fibres.

The implication here is that the supramolecular assemblies generate single polarization domains within each of the micrometre-long ribbons.

Comparison with PVDF-based polymers

Given the high content of the ferroelectric β -phase observed in the OVDF-PAs, we proposed that peptide programming could be generating a higher degree of molecular ordering in the electroactive phase compared with that in PVDF polymers. In the polymeric material, there is a substantial amount of conformationally disordered covalent chains in amorphous regions¹⁵. To verify this hypothesis, we obtained transmission FTIR spectra of dried films of **VDF₆-VEVE** and of commercial ferroelectric polymers. As shown in Fig. 5a, the β -phase content in **VDF₆-VEVE** (normalized for VDF structural units) was indeed found to be 2.4 times higher than that measured for the leading ferroelectric polymer P(VDF-TrFE). Furthermore, we optimized the ferroelectric performance of the OVDF PA films by applying a weak electric field (0.25 V μm^{-1}) during self-assembly (Methods and Supplementary Fig. 55). We observed in these samples large bundles of nanoscale ribbons oriented parallel to the applied electric field (Fig. 5b), whereas no obvious alignment was observed in polymeric samples, even when the applied electric field was increased by an order of magnitude (Extended Data Fig. 3). The corresponding P–E loops for the electric-field-aligned **VDF₆-VEVE** samples revealed a twofold increase in P_r relative to samples prepared in the absence of an electric field and maintained the low level of dielectric loss tangent (less than 0.1; Extended Data Fig. 4). The polymeric samples prepared by the same method did not reveal any evidence of ferroelectricity when an electric field of up to 15 kV cm^{-1} was applied (Fig. 5c and Extended Data Fig. 5), which is not surprising considering the high coercive field of about 500 kV cm^{-1} for these polymeric ferroelectrics^{15,38}. Compared with their polymer counterparts, the electric-field-aligned **VDF₆-VEVE** assemblies generated a remnant polarization strength of the same order of magnitude (about 10 $\mu\text{C cm}^{-2}$ in VDF polymers measured under fields of more than 1,000 kV cm^{-1} (ref. 38) compared with 4 $\mu\text{C cm}^{-2}$ in the assemblies) but can be switched under an electric field two orders of magnitude lower (an E_c of around 5 kV cm^{-1}). This occurs despite the 49 wt% of peptide in our supramolecular assemblies. These observations can be explained by the existence of a great barrier to ferroelectric phase alignment in polymers, as opposed to the facile ordering of self-assembling molecules into ferroelectric supramolecular polymers having a strongly preferred polar axis. We therefore propose that the increased ferroelectric behaviour enabled at very low electric fields is programmed by the self-assembly of peptide segments. We also found that the morphologies and ferroelectric behaviour of the electric-field-aligned OVDF-PA assemblies are stable in air at room temperature for at least ten months (Extended Data Fig. 6).

The ultralow coercive field of OVDF-PA assemblies, relative to the high values in PVDF and even oligomers of VDF (Supplementary Section 6.3), is clearly an interesting and useful feature of these systems. We attribute this in part to the long-range organization of VDF dipoles enabled by the highly one-dimensional array of peptide assemblies that are micrometres in length and hundreds of nanometres in width. This contributes a high degree of favourable cooperativity on domain switching by the external electric field, and emerges as a result of the preferred alignment of long assemblies across the electrode gap when the film is cast from solution under a weak electric field. Because the long axis of the assemblies is parallel to the hydrogen-bond axes of their internal β -sheets, the multiaxial ferroelectric domains exposed to an electric field can select the same direction and thereby avoid torsional forces that would disrupt the secondary structure of peptide domains. We propose that another critical factor leading to low coercive fields is supramolecular motion in the peptide assemblies³⁹; this finding is supported by the presence of disordered peptide segments revealed in FTIR spectra, as well as by the WAXS data discussed earlier (Fig. 2e). Interestingly, we observed a decreasing coercive field and smaller

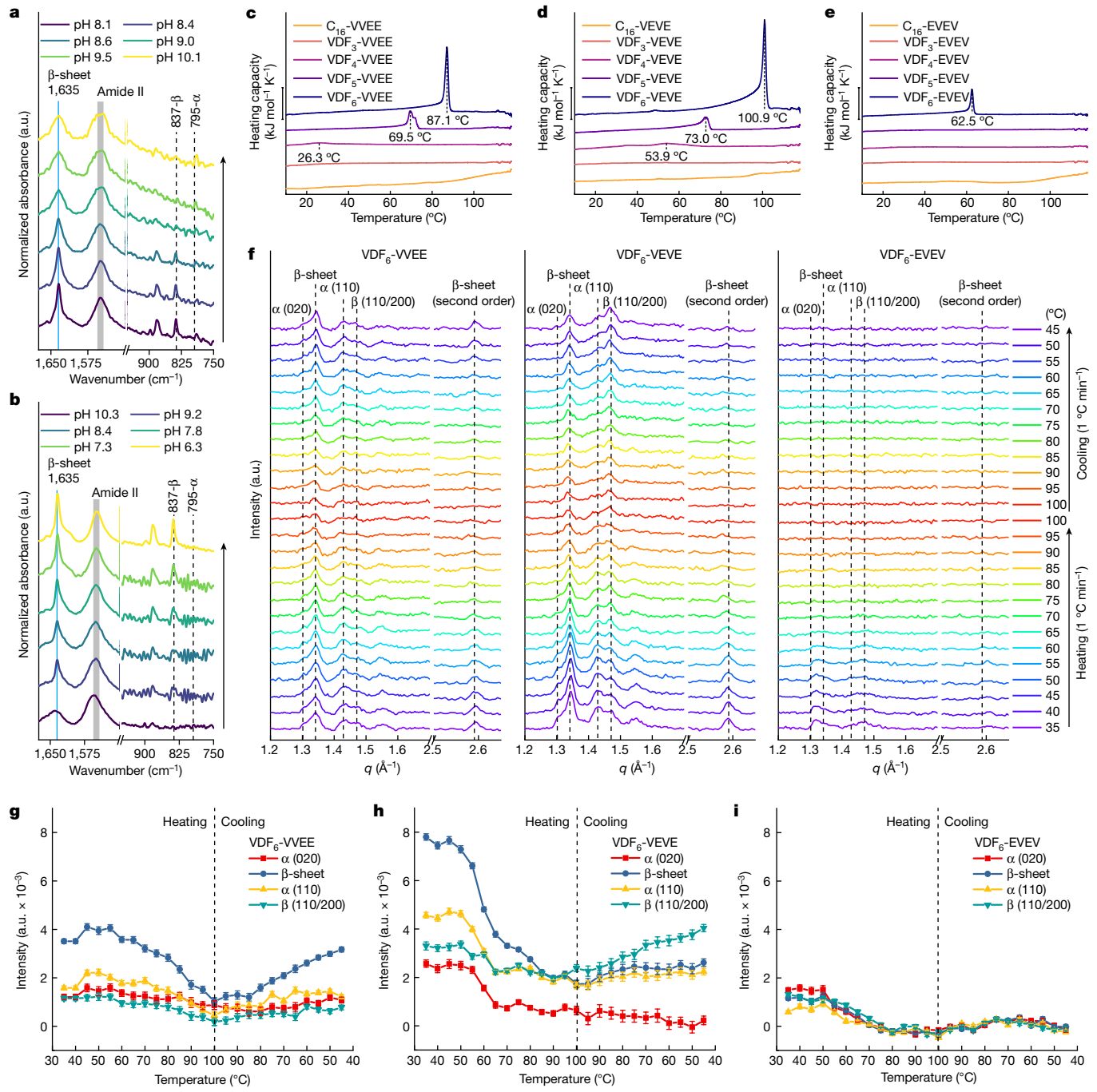


Fig. 4 | Thermodynamic behaviour of OVDF-PA supramolecular assemblies. **a, b**, ATR-FTIR spectra of annealed $\text{VDF}_6\text{-VEVE}$ solutions during pH titration from pH 8.1 to pH 10.1 (**a**) and from pH 10.3 to pH 6.3 (**b**), indicating the position of peaks for amide I absorption in peptide β -sheets and peaks characteristic of the crystalline α and β phases of vinylidene fluoride chains.

c–e, DSC thermograms of annealed $\text{VDF}_6\text{-VVEE}$ (**c**), $\text{VDF}_6\text{-VEVE}$ (**d**) and $\text{VDF}_6\text{-EVEV}$ (**e**) along with the corresponding $\text{C}_{16}\text{-PAs}$ as controls in the first cooling cycle (multi-cycle DSC scans of the $\text{VDF}_6\text{-PAs}$ are shown in Supplementary Fig. 48); y axis scale bars, $2 \text{ kJ mol}^{-1} \text{ K}^{-1}$.

VDF₆-VVEE (left), **VDF₆-VEVE** (middle) and **VDF₆-EVEV** (right) with peak positions indicated: (020) plane at $q = 1.30 \text{ \AA}^{-1}$ and (110) plane at $q = 1.43 \text{ \AA}^{-1}$ for α -phase OVDF, (110)/(200) plane at $q = 1.47 \text{ \AA}^{-1}$ for β -phase OVD, $q = 1.34 \text{ \AA}^{-1}$ for hydrogen bond spacing of β -sheet peptide and its second-order reflection at $q = 2.59 \text{ \AA}^{-1}$.

g–i, Scattering intensity obtained from Gaussian fitting of the scattering patterns in **f** with fixed peak position and full width at half maximum (Supplementary Fig. 51) at different temperatures during heating and cooling cycles. Error bars in **g–i** show the standard error of the fittings. Curves in **a–f** are offset vertically for clarity.

remnant polarization with increasing supramolecular dynamics. This is highest in EVEV, lowest in VEVE and intermediate in VVEE (Fig. 3a–c). Enhanced dynamics could nucleate polarization switching under an external field, becoming most evident in the highly ‘plasticized’ relaxor phase formed by the sequence EVEV.

We have developed supramolecular materials in which vinylidene fluoride peptide amphiphiles organize into ferroelectric structures

across different size scales, which has been a challenge for electroactive fluorinated polymers. The supramolecular system self-assembles into polar nanoscale ribbons with varying domain sizes that organize into bundles at the mesoscale and orient macroscopically in an applied electric field. Tetrapeptides in the amphiphiles that form β -sheet assemblies template long-range ordering of their hydrophobic fluorotelomer segments into a highly functional ferroelectric phase

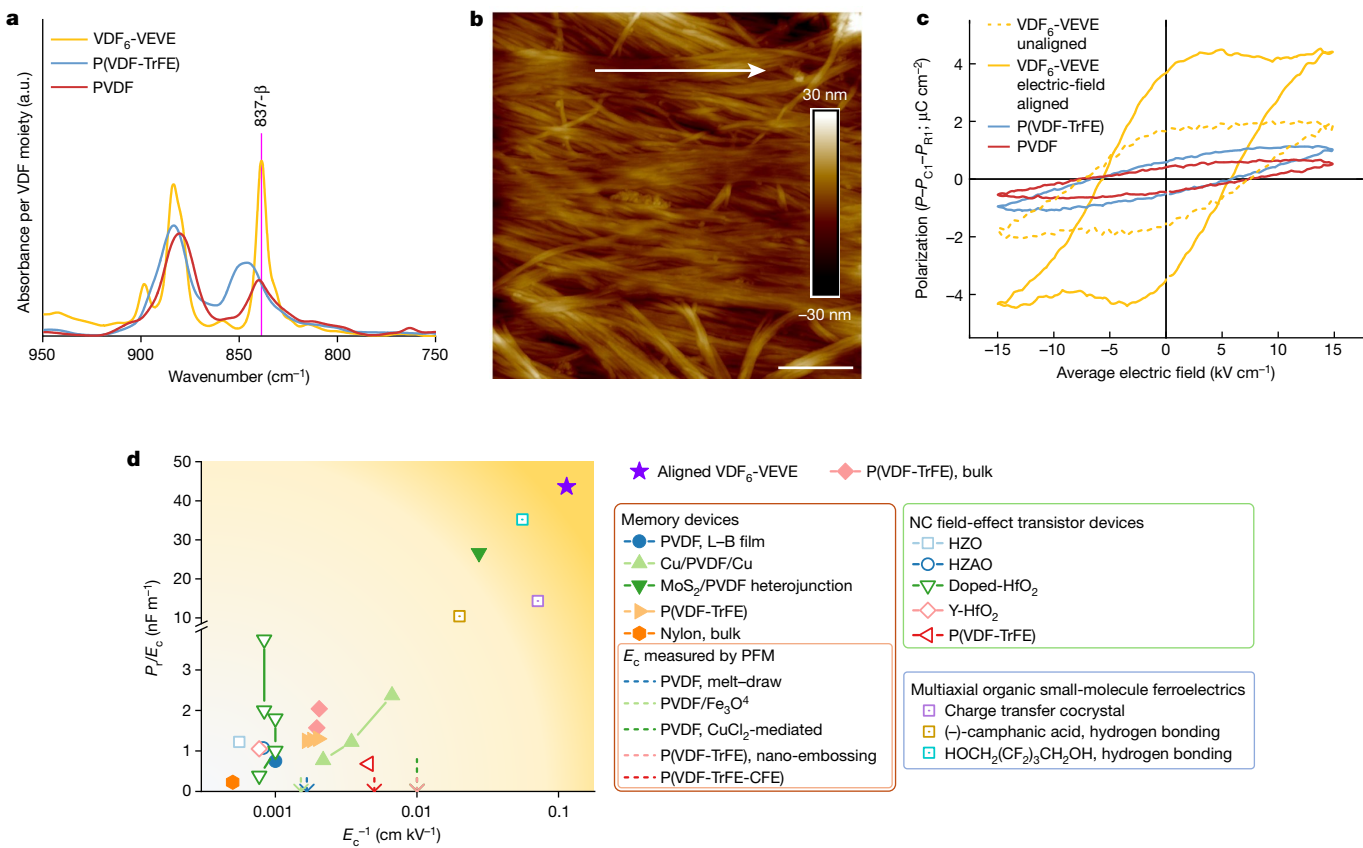


Fig. 5 | Ferroelectric performance of OVDF-PA samples relative to leading commercial ferroelectric polymers. **a**, Transmission FTIR spectra of dried VDF₆-VEVE, P(VDF-TrFE) and PVDF samples on a BaF₂ substrate (full-range spectra are shown in Supplementary Fig. 53). **b**, AFM image of the aligned VDF₆-VEVE nanoscale ribbon bundles within the testing electrode gap (the white arrow indicates the direction of the applied electric field during solution casting of the sample); scale bar, 300 nm. **c**, P-E loops of unaligned and electric-field aligned VDF₆-VEVE, P(VDF-TrFE) and PVDF samples.

d, Comparison of P/E_c versus E_c^{-1} for electric-field aligned VDF₆-VEVE and previously reported ferroelectrics applied in low-voltage memory and state-of-the-art negative-capacitance field-effect transistor devices. Arrowheads indicate that E_c values have previously been determined elsewhere; L-B indicates a Langmuir–Blodgett film; HZO, hafnium–zirconium oxide; HZAO, hafnium–zirconium–aluminum oxide; see Supplementary Table 7 for numerical values of P_r and E_c along with definitions of the acronyms.

that is thermodynamically stable. Relative to polymers, the functionality of these systems includes a strong electroactive response at very low electric fields (Fig. 5c), and a coercive field that is two orders of magnitude lower. We conclude that these attractive properties are linked to the collinear axes of β -sheet hydrogen bonding and the two bistable states of the multiaxial ferroelectric, and also to the inherent dynamics of the molecules in supramolecular polymers. Having access to single nanostructures, such as the peptide amphiphile ribbons investigated here, could lead to ultralow-power devices that can take advantage of transient negative capacitance to overcome the theoretical limit of the ‘Boltzmann tyranny’². This actually requires supramolecular assemblies with a high P_r/E_c ratio and a low E_c value. In this regard, Fig. 5d indicates the values of these two parameters in electric-field-aligned OVDF assemblies compared with other systems. Another promising direction is developing free-standing films of supramolecular systems with preferential orientation either in-plane or out-of-plane, but this may require hybrid materials or specific surface interactions. Furthermore, we hope that our work will inspire further development of water-processable ferroelectrics, for bioelectronics that can also be bioactive and resorbable, or for catalytic applications.

Online content

Any methods, additional references, Nature Portfolio reporting summaries, source data, extended data, supplementary information,

acknowledgements, peer review information; details of author contributions and competing interests; and statements of data and code availability are available at <https://doi.org/10.1038/s41586-024-08041-4>.

- Cheema, S. S. et al. Ultrathin ferroic HfO₂–ZrO₂ superlattice gate stack for advanced transistors. *Nature* **604**, 65–71 (2022).
- Íñiguez, J., Zubko, P., Luk'yanchuk, I. & Cano, A. Ferroelectric negative capacitance. *Nat. Rev. Mater.* **4**, 243–256 (2019).
- Wang, W., Li, J., Liu, H. & Ge, S. Advancing versatile ferroelectric materials toward biomedical applications. *Adv. Sci. Weinh.* **8**, 2003074 (2021).
- Qian, X. et al. High-entropy polymer produces a giant electrocaloric effect at low fields. *Nature* **600**, 664–669 (2021).
- Liu, Y. et al. Ferroelectric polymers exhibiting behaviour reminiscent of a morphotropic phase boundary. *Nature* **562**, 96–100 (2018).
- Qian, X., Chen, X., Zhu, L. & Zhang, Q. M. Fluoropolymer ferroelectrics: multifunctional platform for polar-structured energy conversion. *Science* **380**, eadg0902 (2023).
- Tao, K., Makam, P., Aizen, R. & Gazit, E. Self-assembling peptide semiconductors. *Science* **358**, eaam9756 (2017).
- Horiuchi, S. & Tokura, Y. Organic ferroelectrics. *Nat. Mater.* **7**, 357–366 (2008).
- Tayi, A. S., Kaeser, A., Matsumoto, M., Aida, T. & Stupp, S. I. Supramolecular ferroelectrics. *Nat. Chem.* **7**, 281–294 (2015).
- Horiuchi, S. et al. Above-room-temperature ferroelectricity in a single-component molecular crystal. *Nature* **463**, 789–792 (2010).
- Kholkin, A., Amdursky, N., Bdikin, I., Gazit, E. & Roseman, G. Strong piezoelectricity in bioinspired peptide nanotubes. *ACS Nano* **4**, 610–614 (2010).
- Miyajima, D. et al. Ferroelectric columnar liquid crystal featuring confined polar groups within core-shell architecture. *Science* **336**, 209–213 (2012).
- Tayi, A. S. et al. Room-temperature ferroelectricity in supramolecular networks of charge-transfer complexes. *Nature* **488**, 485–489 (2012).
- Kawai, H. The piezoelectricity of poly(vinylidene fluoride). *Jpn. J. Appl. Phys.* **8**, 975 (1969).
- Lovinger, A. J. Ferroelectric polymers. *Science* **220**, 1115–1121 (1983).

16. Guo, M. et al. Toroidal polar topology in strained ferroelectric polymer. *Science* **371**, 1050–1056 (2021).
17. Zhang, H.-Y., Tang, Y.-Y., Shi, P.-P. & Xiong, R.-G. Toward the targeted design of molecular ferroelectrics: modifying molecular symmetries and homochirality. *Acc. Chem. Res.* **52**, 1928–1938 (2019).
18. Narayanan, A. et al. Ferroelectric polarization and second harmonic generation in supramolecular cocrystals with two axes of charge-transfer. *J. Am. Chem. Soc.* **139**, 9186–9191 (2017).
19. Kimura, K. & Ohigashi, H. Polarization behavior in vinylidene fluoride-trifluoroethylene copolymer thin films. *Jpn. J. Appl. Phys.* **25**, 383 (1986).
20. Herman, Umemoto, S., Kikutani, T. & Okui, N. Chain length effects on crystal formation in vinylidene fluoride oligomers. *Polym. J.* **30**, 659–663 (1998).
21. Yoshida, Y., Ishida, K., Ishizaki, K., Horiuchi, T. & Matsushige, K. Effect of substrate temperature on molecular orientation in evaporated thin films of vinylidene fluoride oligomer. *Jpn. J. Appl. Phys.* **36**, 7389 (1997).
22. Noda, K. et al. Remanent polarization of evaporated films of vinylidene fluoride oligomers. *J. Appl. Phys.* **93**, 2866–2870 (2003).
23. García-Iglesias, M. et al. A versatile method for the preparation of ferroelectric supramolecular materials via radical end-functionalization of vinylidene fluoride oligomers. *J. Am. Chem. Soc.* **138**, 6217–6223 (2016).
24. Hartgerink, J. D., Beniash, E. & Stupp, S. I. Self-assembly and mineralization of peptide-amphiphile nanofibers. *Science* **294**, 1684–1688 (2001).
25. Tantakitti, F. et al. Energy landscapes and functions of supramolecular systems. *Nat. Mater.* **15**, 469–476 (2016).
26. Cui, H., Cheetham, A. G., Pashuck, E. T. & Stupp, S. I. Amino acid sequence in constitutionally isomeric tetrapeptide amphiphiles dictates architecture of one-dimensional nanostructures. *J. Am. Chem. Soc.* **136**, 12461–12468 (2014).
27. Paramonov, S. E., Jun, H.-W. & Hartgerink, J. D. Self-assembly of peptide-amphiphile nanofibers: the roles of hydrogen bonding and amphiphilic packing. *J. Am. Chem. Soc.* **128**, 7291–7298 (2006).
28. Muraoka, T., Cui, H. & Stupp, S. I. Quadruple helix formation of a photoresponsive peptide amphiphile and its light-triggered dissociation into single fibers. *J. Am. Chem. Soc.* **130**, 2946–2947 (2008).
29. Kobayashi, M., Tashiro, K. & Tadokoro, H. Molecular vibrations of three crystal forms of poly(vinylidene fluoride). *Macromolecules* **8**, 158–171 (1975).
30. Shibu, B. et al. Distinct β -sheet structure in protein aggregates determined by ATR-FTIR spectroscopy. *Biochemistry* **52**, 5176–5183 (2013).
31. Sangji, M. H. et al. Supramolecular interactions and morphology of self-assembling peptide amphiphile nanostructures. *Nano Lett.* **21**, 6146–6155 (2021).
32. Hasegawa, R., Takahashi, Y., Chatani, Y. & Tadokoro, H. Crystal structures of three crystalline forms of poly(vinylidene fluoride). *Polym. J.* **3**, 600–610 (1972).
33. Yang, L. et al. Novel polymer ferroelectric behavior via crystal isomorphism and the nanoconfinement effect. *Polymer* **54**, 1709–1728 (2013).
34. Zhang, Q. M., Bharti, V. & Zhao, X. Giant electrostriction and relaxor ferroelectric behavior in electron-irradiated poly(vinylidene fluoride-trifluoroethylene) copolymer. *Science* **280**, 2101–2104 (1998).
35. Chen, X. et al. Relaxor ferroelectric polymer exhibits ultrahigh electromechanical coupling at low electric field. *Science* **375**, 1418–1422 (2022).
36. Scott, J. F. Ferroelectrics go bananas. *J. Phys. Condens. Matter* **20**, 021001 (2008).
37. Leung, C.-Y. et al. Crystalline polymorphism induced by charge regulation in ionic membranes. *Proc. Natl. Acad. Sci. USA* **110**, 16309–16314 (2013).
38. Furukawa, T. Ferroelectric properties of vinylidene fluoride copolymers. *Phase Transit.* **18**, 143–211 (1989).
39. Álvarez, Z. et al. Bioactive scaffolds with enhanced supramolecular motion promote recovery from spinal cord injury. *Science* **374**, 848–856 (2021).

Publisher's note Springer Nature remains neutral with regard to jurisdictional claims in published maps and institutional affiliations.

Springer Nature or its licensor (e.g. a society or other partner) holds exclusive rights to this article under a publishing agreement with the author(s) or other rightsholder(s); author self-archiving of the accepted manuscript version of this article is solely governed by the terms of such publishing agreement and applicable law.

© The Author(s), under exclusive licence to Springer Nature Limited 2024

Article

Methods

Materials

All the chemicals we used were purchased from Sigma-Aldrich or Thermo Fisher Scientific, and were used without any purification unless specified. 1,1-Difluoroethylene (VDF, 99%) gas was purchased from SynQuest Labs. Ethylene (99.9%) gas was purchased from Airgas. The bis(4-*tert*-butylcyclohexyl) peroxydicarbonate initiator was a gift from United Initiators and was used as supplied. PVDF (182702-5 G) and P(VDF-TrFE) (TrFE/VDF 25:75 mol%, Solvay Solvane 250/P400, 900904-10 G) were purchased from Sigma-Aldrich.

Preparation of PA solutions. The PAs were first dissolved in 1,1,1,3,3,3-hexafluoro-2-propanol (HFIP) to disassemble any β -sheet-containing structures in the lyophilized powders, allowing for normalization of the fresh solutions. After evaporation of HFIP, the PA powders were dissolved at the desired concentration in deionized water containing 1 equivalent of sodium hydroxide followed by a water-bath sonication for 15 min. The solution was then titrated to neutral pH (6.8–7.0 by Hydron pH paper) using 100 mM sodium hydroxide stock solution with an excess of around 0.2 equivalents of sodium hydroxide. Solutions were then annealed at 80 °C unless specified otherwise in a water bath (approximately 3 l) for 1 h followed by slow cooling to room temperature to eliminate kinetically trapped states in the samples and produce thermodynamically stable assemblies.

AFM. AFM experiments were done at room temperature using a Veeco Dimension icon scanning probe microscope (Veeco) and a Nanoscope V Controller (Bruker). The SNL-10-A probes (nominal tip radius of 2 nm and spring constant of 0.35 N m⁻¹; Bruker) were used in liquid-state experiments with ScanAsyst in fluid imaging mode (Peakforce Force Tapping) at 2 kHz with an amplitude of 50 nm. The ScanAsyst-air probes (normal tip radius of 2 nm and spring constant of 0.4 N m⁻¹; Bruker) were used in dried-state experiments using the ScanAsyst in air imaging mode (Peakforce Force Tapping) at 2 kHz with an amplitude of 150 nm. Height measurements of PA assemblies were done on Nanoscope Analysis software with the substrate height subtracted.

TEM and SAED. TEM and SAED experiments were done on a JEOL ARM300F field-emission transmission electron microscope equipped with a Gatan OneView detector, using an accelerating voltage of 300 kV. Samples for TEM were diluted to around 0.5–1.0 mM with 10 mM NaCl_{aq} and immediately cast on glow-discharged carbon-coated TEM grids (CF300-Cu-UL, Electron Microscopy Sciences). The grids were then negatively stained with 2 wt% uranyl acetate solution. For SAED, a 10 mM PA solution was directly cast on glow-discharged carbon-coated TEM grids, then wicked with filter paper. After drying, the samples were washed with 5 μ l deionized water followed by wicking and drying. For the SAED of **VDF₆-EVEV** measured under cryogenic conditions, the samples were cast on the grids at 4 °C (below the freezing temperature of 37.2 °C measured for these assemblies). The samples were then loaded on a Gatan 626 cryo-transfer holder and were cooled in the TEM column to –180 °C before imaging and SAED measurements.

WAXS/SAXS. Solution X-ray measurements were done at Beamline 5-ID-D in the DuPont-Northwestern-Dow Collaborative Access team (DND-CAT) Synchrotron Research Center at the Advanced Photon Source, Argonne National Laboratory. An X-ray energy of 17 keV was selected using a double-crystal monochromator. The scattering vector q is defined as $q = (4\pi/\lambda) \sin \theta$, where 2θ is the total scattering angle. Samples were oscillated with a syringe pump during exposure to prevent beam damage, and background samples containing 10 mM NaCl_{aq} were also collected. The WAXS traces were subjected to multipoint baseline correction to detect Bragg reflections.

For variable-temperature (VT) measurements, the 20 mM OVDF-PA solutions and 20 mM NaCl buffer were sealed in 1.5 mm quartz capillaries using UV-curing glue. Starting at 35 °C, the solution was heated in 5 °C steps, each at 10 °C min⁻¹. The 0.5 min heating period was followed by 1 min equilibration time and subsequent data acquisition. Buffer-filled capillary scattering data were recorded with the same VT protocol to be used for background subtraction and baseline correction.

FTIR spectroscopy. The ATR FTIR spectroscopy was done on a ThermoNicolet iS50 spectrometer equipped with a Pike MIRacle Single Reflection ATR module. Measurements on liquid samples were obtained by adding 0.5 μ l PA solutions covering the crystal surface of the ATR module, and the background signal was collected using a 10 mM NaCl solution (measurements were also obtained on air-dried samples). The vibrational bands at 837 cm⁻¹ are known to be associated with CH₂ rocking in either β -phase or γ -phase PVDF, depending on which dominant absorption peaks are observed (1,275 cm⁻¹ is β -phase and 1,234 cm⁻¹ is γ -phase). Because the absorption peak at 1,275 cm⁻¹ is always dominant and an obvious absorption peak at 1,234 cm⁻¹ was not observed in our experiments, we assigned the vibration bands at 837 cm⁻¹ to β -phase OVDF. For the ATR-FTIR spectra of **VDF₆-VEVE** liquid samples during pH titration, 20 mM annealed PA solutions were diluted to 10 mM, then 50 mM NaOH solutions with 0.08, 0.16, 0.44, 0.72, 1.0 and 1.68 equivalents of base were added to obtain pH values of 8.1, 8.4, 8.6, 9.0, 9.5 and 10.1, respectively, as measured by a pH meter. For the acidic titration experiments, 20 mM annealed **VDF₆-VEVE** solutions were diluted to 10 mM, and a 100 mM NaOH solution with 1.8 equivalents of base was added to disrupt the β -sheet structures until an absorption peak for VDF crystals was no longer observed. Then 100 mM HCl solutions with 0, 0.5, 1.0, 1.4, 1.6 and 2.0 equivalents of acid were added to obtain different pH values of 10.3, 9.2, 8.4, 7.8, 7.3 and 6.3, as measured by a pH meter, respectively. The absorbance intensities of the spectra were normalized to the maximum characteristic band of amide II (1,500–1,600 cm⁻¹). Transmission-mode FTIR of PVDF, P(VDF-TrFE) and **VDF₆-VEVE** dried films were done by casting 19.3 mg ml⁻¹ *N,N*-dimethylformamide (DMF) solutions of the polymers and 20 mM annealed aqueous solution of **VDF₆-VEVE** on a 1 mm thick BaF₂ substrate (MSE Supplies LLC), and the samples were annealed at 80 °C and 135 °C for 4 h to remove the DMF and increase the crystallinity of the polymers. We assumed that the dried samples had similar mass densities, and the infrared absorbance intensities of the spectra were normalized by the film thicknesses and mass fractions of the VDF monomers (Supplementary Table 4) to quantify the crystal phase content per VDF moiety in the samples.

To prepare the aligned **VDF₆-PA** assembly samples for the polarized transmission FTIR, polydimethylsiloxane (PDMS) embossing stamps were prepared using a plane ruled reflective grating (Edmund, 300 grooves per millimetre, 12.5 × 25 mm, blaze angle of 26.7°) as the template. The PDMS stamps were then placed on a 0.5 mm thick n-type germanium wafer (MSE Supplies LLC) to create microchannels. The freshly dissolved 10 mM **VDF₆-PA** solutions were prepared after HFIP treatment and immediately added to one edge of the PDMS stamps with the openings of the microchannels. After the solution filled the microchannels by the capillary effect, the wafer was sealed in a glass bottle containing some water to maintain high humidity and then annealed at 80 °C in a water bath (approximately 3 l) for 1 h followed by slow cooling to room temperature. Finally, the samples were dried under vacuum and the PA assemblies were left on the wafer after removing the PDMS stamp. Transmission FTIR was then performed with a polarizer inserted in the light path and the electric field of the incident infrared laser was fixed parallel (0°) or perpendicular (90°) to the long axes of the PA ribbons.

DSC. The annealed 20 mM PA solutions were diluted to 1.25 mM in water to prepare samples for DSC measurements. DSC thermograms were obtained using a Nano DSC instrument (TA Instruments, model 602001) at a constant pressure (6.0 atm) with the sample matched

against 1.25 mM NaCl buffer in the reference cell. Samples were cooled to 5 °C then equilibrated for 600 s, followed by three alternating heating and cooling cycles from 5 °C to 120 °C at a scan rate of 1 °C min⁻¹. A 600 s equilibration period was added before each heating and cooling cycle. The cooling data were analysed and converted to molar heating capacity using NanoAnalyze Data Analysis, v.3.12.0 (TA Instruments).

P-E loop measurements and corresponding sample preparation. Annealed 20 mM sample solutions were deposited on a silicon testing chip with a 300 nm thick SiO₂ insulation layer and photolithographically patterned platinum electrodes with 2 μm channel width (Ossila, S403A1) (the cross-section of the electrode is 1 mm wide and 100 nm thick). The testing channel was coated with a 600–800 nm thick sample, as measured by AFM after evaporation of the solvent. The samples were dried under high vacuum (2×10^{-7} mbar) overnight before the electrical tests. To avoid the influence of air and moisture, the chips were sealed on the testing board (Ossila, E481) and the boards were sealed in a nitrogen bag during the measurements. The P-E loops were measured using a ferroelectric tester (Radiant Technologies Precision LC) at room temperature unless specified otherwise. Double bipolar triangle waveforms were applied with a single loop period of 50 ms, a pre-loop delay between the two loops of 10 ms and maximum voltages of around 0.8–4.5 V. The final loop was recorded as the original P-E loop data (the resistance of the samples was measured using the same set-up). A DC voltage of around 1–5 V was applied and the leakage current was recorded for 10 s until the polarization process was complete. The frequency-domain impedance spectrum was measured using AutoLab PGSTAT-128N (voltage amplitude of 0.1–0.3 V) and Solartron 1260 (voltage amplitude of 0.2–1.0 V) at room temperature. The linear capacitance C_1 was obtained from the high-frequency (100 kHz) measurements to exclude the contribution of ferroelectric polarization. The ferroelectric component was obtained after subtracting the contribution of C_1 and linear resistance R_1 from the original P-E loop (Supplementary Fig. 24). Polarization strengths measured on a blank substrate show constant stray capacitance, which can be subtracted with negligible residual error in the final P-E loops (Supplementary Fig. 18). High-temperature P-E loop measurements were performed with the testing board encapsulated in a heating chamber (Supplementary Fig. 32). A micro-thermocouple was attached on the back side of the testing chip to monitor the sample temperature.

To obtain the alignment of the **VDF₆-VEVE** assemblies along the applied electric field crossing the electrode channel, **VDF₆-VEVE** was dissolved at a concentration of 5 mM in 70:30 H₂O:HFIP (v/v) to disrupt the β-sheet structures. The solution was filled into a semi-closed liquid cell prepared by a coverslip on a testing chip mounted on a heating stage (Supplementary Fig. 55). Probe electrodes were used to apply a voltage of 0.5 V to the testing channels so an average electric field of 0.25 V μm⁻¹ was generated between the 2 μm electrode gap at the bottom of solutions. Then, samples were heated up to 80 °C (at about 15 °C min⁻¹) in an argon atmosphere and kept for 30 min before cooling to room temperature (at about 1 °C min⁻¹). Most of the liquid inside the semi-closed cell was evaporated after the annealing process and the coverslip was removed to let the sample dry in air for another 30 min before turning off the electric field. Finally, the samples were dried in a vacuum (2×10^{-7} mbar) overnight before the electrical tests. For the comparison with ferroelectric polymers, PVDF and P(VDF-TrFE) solutions were prepared by dissolving the polymer powder in DMF with the same concentration of 19.3 mg ml⁻¹ as 20 mM **VDF₆-PA** aqueous solutions and stirred overnight. The solutions were cast on the testing chip with the same electric field of 0.25 V μm⁻¹ applied to the 2 μm electrode gap. Samples were heated to 80 °C in an argon atmosphere and kept for 30 min to evaporate the DMF and then heated to 135 °C and kept for 4 h to improve the crystallinity before cooling to room temperature (about -1 °C min⁻¹) and turning off the applied electric field. The samples were then kept in a vacuum (2×10^{-7} mbar) overnight to

remove the residual DMF before electrical tests. The polymer samples cast in an electric field of 2.5 V μm⁻¹ were also prepared to induce more of the ferroelectric phase in the PVDF.

Calibration of coercive fields and polarization strengths. To calibrate the measured coercive field, solution-cast PVDF films with similar thicknesses (around 650 nm) to the PA samples (Supplementary Fig. 57) were prepared on the in-plane electrodes following the procedures described above under an average electric field of 2.5 V μm⁻¹ to induce β-phase crystallization. The samples were thermally annealed at 120 °C in vacuum for 12 h before measurements. High-field P-E loops of P(VDF-TrFE) films on the in-plane electrodes were also measured to verify the calibration method. Calibration measurements using PVDF indicated that the coercive field measured on the 2 μm in-plane electrode gap was about 35% lower than the value typically measured under uniform electric fields (Supplementary Fig. 19). High-field P-E loops of P(VDF-TrFE) films (containing 75 mol% VDF units) on the in-plane electrodes also showed a coercive field close to the reported values and a similar calibration coefficient of 1.43 (Supplementary Fig. 19), which validates our calibration method.

For the calibration of polarization strengths measured using the in-plane electrodes, a standard solution-cast P(VDF-TrFE) film was prepared on a glass substrate coated with indium tin oxide (surface resistivity, 70–100 Ω sq⁻¹). The sample was annealed at 120 °C for 12 h before electrical measurements, and the thickness of the sample (around 1.1 μm) was measured by AFM. A circular gold contact with a diameter of 2 mm and a thickness of 200 nm was then sputter-coated as the top parallel plate electrode. High-field P-E loops of the standard P(VDF-TrFE) film showed the typical coercive fields around 500 kV cm⁻¹ and a saturated polarization of 10 μC cm⁻² (Supplementary Fig. 20b). The low-field P-E loops (Supplementary Fig. 20c) of the standard sample were measured to calibrate the polarization strengths of the P-E loops measured on the in-plane electrodes. Similarly, the P(VDF-TrFE) samples coated on the 2 μm in-plane electrode gap were prepared by the same solution casting method followed by annealing at 120 °C for 12 h. To quantify the edge effects of the in-plane electrodes, six samples with film thicknesses from 100 nm to 1,250 nm were prepared and confirmed by AFM (Supplementary Fig. 21). Because of the low polarization signal of the polymer samples, low-field measurements of the P(VDF-TrFE) samples were performed in a grounded metal chamber to further reduce electromagnetic noise in the measured P-E loops (Supplementary Fig. 22 and Supplementary Table 3). Finally, the calibration coefficients of polarization strength were calculated as the ratios of the electric susceptibility of the standard P(VDF-TrFE) film measured by parallel plate electrodes and the values of the P(VDF-TrFE) samples measured using the in-plane electrodes (Supplementary Fig. 23). Because of the measured thicknesses of PA (600–800 nm) and polymer (700–900 nm) samples prepared on the substrate, the polarization strengths ($P - P_{C1} - P_{R1}$) of the P-E loops were multiplied by calibration coefficients equal to 0.33 and 0.28, respectively.

Variable-temperature dielectric constant measurements. Thin films of the PA samples with a thickness of 20–40 μm, measured using a thickness gauge (Mitutoyo), were prepared by casting 20 mM annealed solutions on a gold-plated silicon wafer (Supplementary Fig. 30) followed by the evaporation of water and dried in a vacuum overnight at room temperature. The thicknesses of the PA samples are shown in Supplementary Table 4. The variable-temperature frequency-domain impedance measurements were performed using AutoLab PGSTAT-128N at a voltage amplitude of 0.5 V. A spring test probe with a spherical tip (0.6 mm diameter, Ni plated on Au, SFENG) was applied as the top electrode, and the effective electrode area (0.588 mm²) was determined by performing the dielectric-constant measurement on a 25 μm polyimide standard film (DuPont, Kapton) (Supplementary Fig. 30). The samples were mounted on a heating stage with a micro-thermocouple

Article

nearby and the sample cell was blown with argon gas during experiments. Before the measurements, the samples were heated to 40 °C for 30 min to remove moisture, and then a temperature sweep from 22 °C to 120 °C was applied at a scanning rate of 1 °C min⁻¹ and the impedance was measured from 1 Hz to 100 kHz at every step of 2 °C. Then the complex impedance data were converted to complex capacitance and the dielectric constants of the samples were calculated according to the real part of the complex capacitance.

PFM. Porous AAO films with a conductive aluminium substrate (InRedox), 300 nm pore diameter and 2 μm thickness were used as the template to assemble the OVDF-PA nanostructures perpendicular to the conductive substrate. Freshly dissolved 20 mM OVDF-PA aqueous solution after HFIP treatment was added to the AAO substrate. The AAO substrate immersed in PA solution was then sealed in a glass bottle containing some water to maintain high humidity and then annealed at 80 °C in a water bath (approximately 3 l) for 1 h followed by slow cooling to room temperature. The PA solution on the surface of the substrate was removed by blowing nitrogen gas, and the above steps were repeated once. Finally, the samples were dried in a vacuum, and aligned PA assemblies were left inside the pore channels with the elongation axes aligned in the out-of-plane direction. The AFM morphology measurements were done to confirm that the pore channels were filled and that the PA on the surface of the samples had been removed.

The PFM measurements were performed using the AFM instrument. The conductive PFTUNA probes (Pt/Ir coating, nominal tip radius 25 nm, spring constant 0.4 N m⁻¹, Bruker) were used to perform high-resolution morphology measurements using ScanAsyst in air imaging mode (Peak-force Force Tapping) and electromechanical measurements using ramp mode in the PFM Optimized Vertical Domains Operation workspace on the dried-state samples in AAO films (the deflection sensitivity of the probe was measured against a sapphire standard in air as 41.61 nm V⁻¹). The PFM loops were measured with a contact force of 8.6 nN, a tip bias voltage swept between ±10 V at 20 V s⁻¹ (0.5 Hz) to polarize the sample, and a 50 kHz oscillating driving voltage with an amplitude of 1–5 V (5 V if not specified) applied to the conductive substrate to induce electromechanical actuation without disturbing the orientation of the ferroelectric domains. The PFM loops were measured on the surfaces of filled pores and the surrounding aluminium oxide walls (Supplementary Figs. 34–36) to validate the measured electromechanical response of the PA samples in the pores. The final PFM amplitude curves of the VDF₆-PA samples were obtained by subtraction of the PFM amplitude curves of the surrounding aluminium oxide wall testing points, as shown in Supplementary Figs. 34–36. Verification tests were performed on the aluminium oxide walls using different contact forces (2.9, 8.6, 14.3, 20.0 and 25.7 nN) and sweeping frequencies of tip bias (0.1, 0.2, 0.5, 1.0 and 2.0 Hz) to rule out any effects of sample surface charge and electromigration of ions, respectively (Supplementary Fig. 37).

Data availability

The datasets generated during and/or analysed during the current study are available from the corresponding authors.

40. Hung, A. M. & Stupp, S. I. Understanding factors affecting alignment of self-assembling nanofibers patterned by sonication-assisted solution embossing. *Langmuir* **25**, 7084–7089 (2009).

Acknowledgements This work was primarily supported by the US Department of Energy (DOE), Office of Science, Office of Basic Energy Sciences (BES) award DE-SC0020884. Further support for transmission electron microscopy, electron diffraction and X-ray scattering studies was from the Center for Bio-Inspired Energy Science, an Energy Frontier Research Center funded by the DOE-BES, award DE-SC0000989. We acknowledge the use of the following core facilities at Northwestern University: the REACT Core facility acknowledges funding from the DOE-BES Catalysis Science programme (DE-SC0001329) used for the purchase of the Parr reactor system; the Peptide Synthesis Core Facility of the Simpson Querrey Institute, which has received support from the Soft and Hybrid Nanotechnology Experimental Resource (NSF ECCS-1542205); the Integrated Molecular Structure Education and Research Center, which received support from the Soft and Hybrid Nanotechnology Experimental Resources (NSF ECCS-1542205); the Keck-II facility and the BioCryo facility of the Atomic and Nanoscale Characterization Experimental Center, which received support from the Soft and Hybrid Nanotechnology Experimental (SHyNE) resource (NSF ECCS-1542205). The X-ray experiments were done at the DuPont-Northwestern-Dow Collaborative Access Team located at sector 5 of the Advanced Photon Source. DND-CAT is supported by Northwestern University, the Dow Chemical Company and DuPont de Nemours. This research used the resources of the Advanced Photon Source, a US DOE Office of Science user facility operated for the DOE Office of Science by Argonne National Laboratory under contract DE-AC02-06CH11357. Part of the data collection for X-ray scattering was performed at the LiX beamline (16-ID) at NSLS-II. The LiX beamline is part of the Center for Biomolecular Structure (CBMS), which is primarily supported by the National Institutes of Health, National Institute of General Medical Sciences (NIGMS) through a P30 Grant (P30GM133893), and by the DOE Office of Biological and Environmental Research (KP1605010). LiX also received additional support from NIH Grant S10 OD012331. As part of NSLS-II, a national user facility at Brookhaven National Laboratory, work performed at the CBMS is supported in part by the US Department of Energy, Office of Science, Office of Basic Energy Sciences Program under contract number DE-SC0012704. We thank United Initiators for the gift of bis(4-tert-butyl cyclohexyl) peroxydicarbonate initiator. We thank N. Schweitzer for designing the gas dosing system and facilitating the OVDF synthesis in the REACT core facility. We thank P. Smets (Northwestern University) for assistance with SAED. Molecular graphics were created by M. Seniw in the Analytical bioNanoTechnology Equipment Core Facility of the Simpson Querrey Institute for BioNanotechnology at Northwestern University, which receives partial support from the SHyNE resource (NSF ECCS-2025633).

Author contributions Y.Y. designed and synthesized the OVDF-PA molecules, did most of the experiments, analysed the data and wrote the paper. H.S. did the TEM/SAED and X-ray scattering measurements. S.A.E. and R.Q. contributed to the X-ray scattering measurements. L.C.P. discussed the data and helped to write the paper. S.I.S. supervised the research and also wrote the paper. All authors contributed to the data analysis and preparation of the paper.

Competing interests S.I.S. and Y.Y. are co-inventors on a patent application related to this work filed by Northwestern University (patent no. 63/480,083, filed on 16 January 2023). The authors declare that they have no other competing interests.

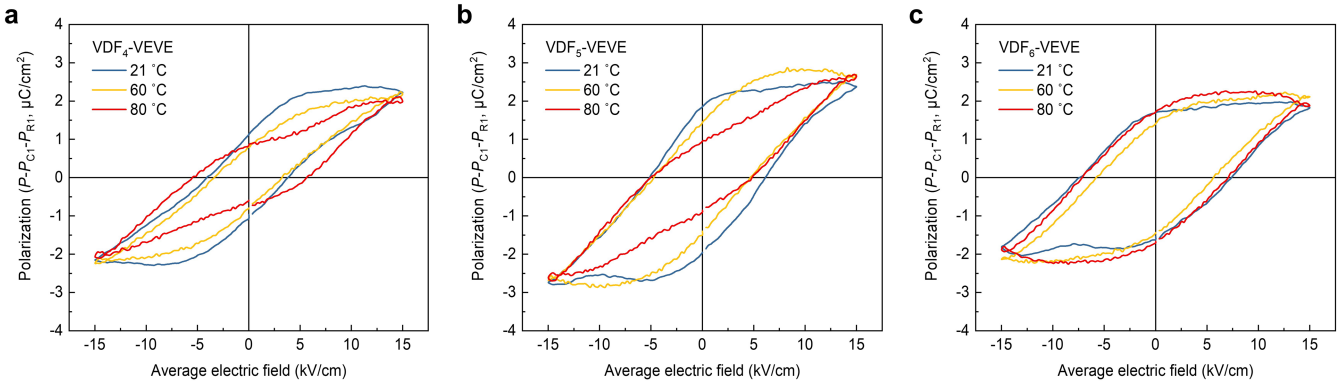
Additional information

Supplementary information The online version contains supplementary material available at <https://doi.org/10.1038/s41586-024-08041-4>.

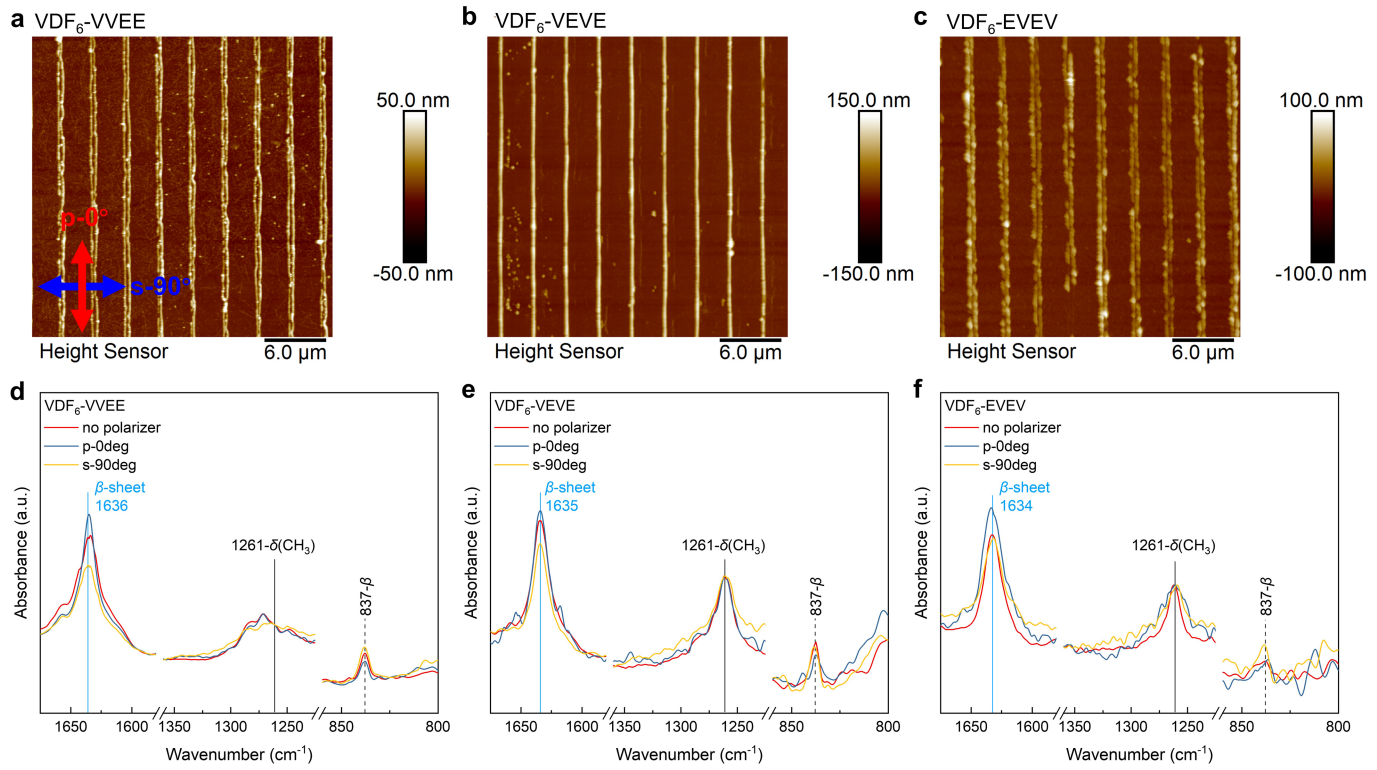
Correspondence and requests for materials should be addressed to Samuel I. Stupp.

Peer review information *Nature* thanks the anonymous reviewers for their contribution to the peer review of this work.

Reprints and permissions information is available at <http://www.nature.com/reprints>.

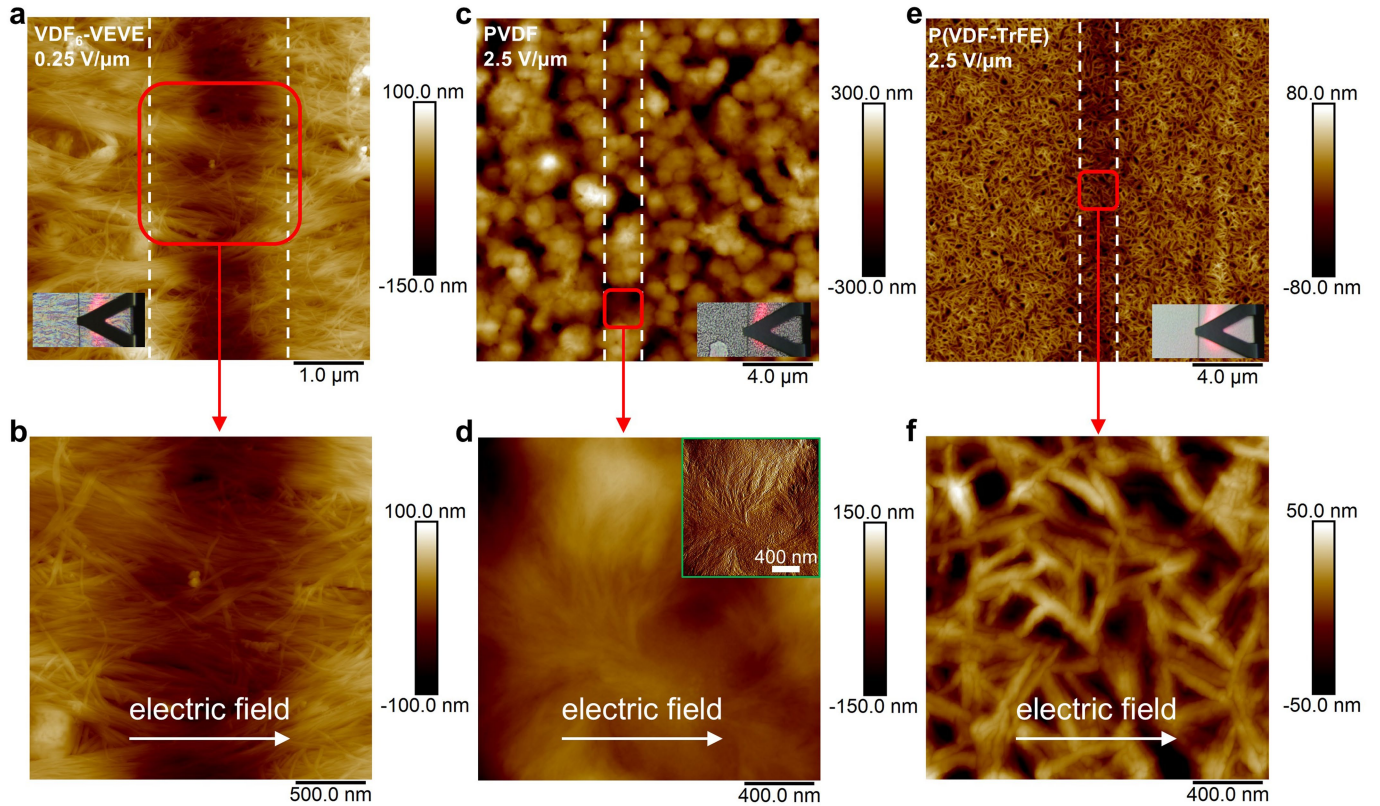


Extended Data Fig. 1 | High-temperature ferroelectricity of OVDF-VEVE assemblies. **a-c**, P-E loops of VDF₄-VEVE (a), VDF₅-VEVE (b), and VDF₆-VEVE (c) samples measured at 21 °C, 60 °C, and 80 °C using the experimental setup shown in Supplementary Fig. 32.



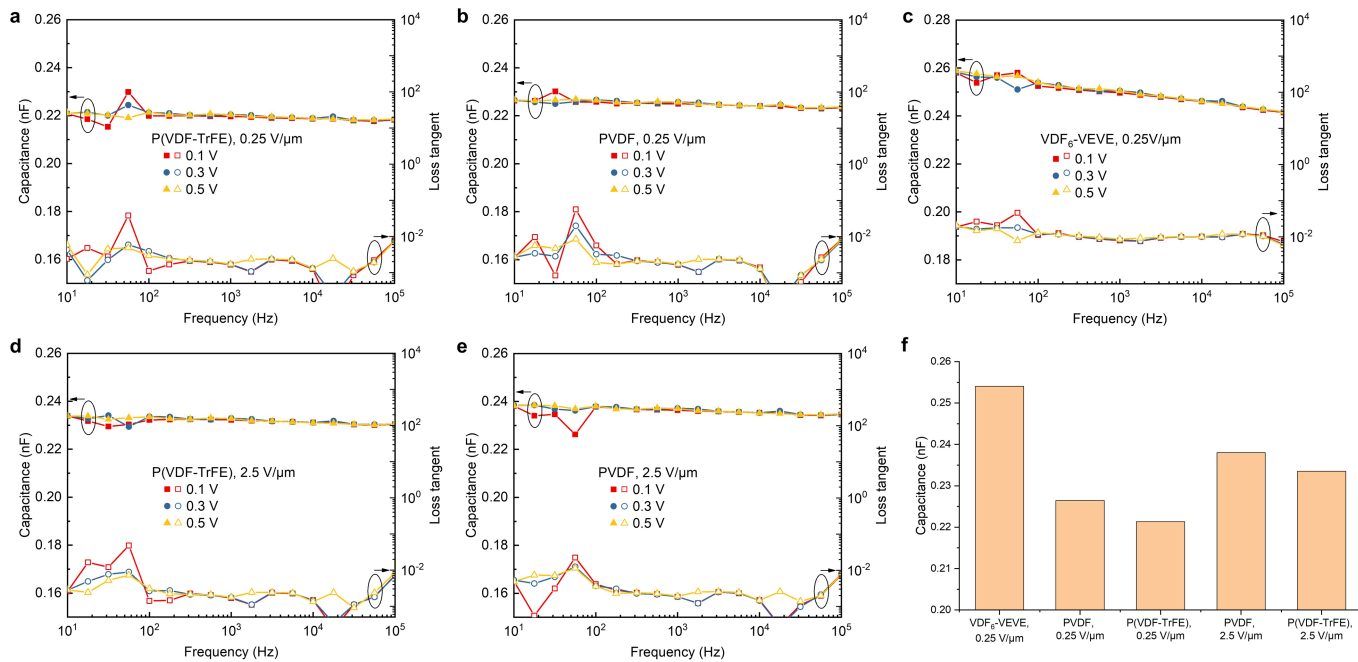
Extended Data Fig. 2 | Polarized transmission FTIR of the aligned VDF_6 -PA fibers. **a-c**, AFM images of the aligned **(a)** VDF_6 -VVEE, **(b)** VDF_6 -VEVE, and **(c)** VDF_6 -EVEV fibers prepared by solution embossing on a germanium wafer. **d-f**, Non-polarized and polarized transmission FTIR spectra on the aligned **(d)** VDF_6 -VVEE, **(e)** VDF_6 -VEVE, and **(f)** VDF_6 -EVEV fibers with the electric field of the incident IR parallel (p-polarized) or perpendicular (s-polarized) relative to the elongation axis of the PA assemblies. Spectra were normalized to the characteristic band of isotropic bending of CH_3 group $\delta(\text{CH}_3)$ at 1261 cm^{-1} . The absorption band of amide C = O stretching vibration $\nu(\text{C} = \text{O})$ near 1635 cm^{-1} with the transition dipole moment parallel to the hydrogen-bonding direction and CF_2 rocking ($\text{r}(\text{CF}_2)$) at 837 cm^{-1} with the dipole transition moment

perpendicular to the polar *b* axis of β -phase OVDF are labeled. The amide C = O stretching vibration with the transition dipole moment parallel to the hydrogen-bonding direction is enhanced in p-polarized IR and weakened in the orthogonal polarization direction. This indicates that the hydrogen-bonding direction of the β -sheets is parallel to the elongation axis of the PA fibers, consistent with previous research on similar PA nanostructures⁴⁰. The intensities of the absorption peak of CH_2 rocking (837 cm^{-1}) vibration with the dipole transition moment perpendicular to the polar *b* axis of β -phase OVDF display the opposite trend, indicating that the *b* axis of the β -phase OVDF crystal is parallel to the elongation axis (i.e., hydrogen-bonding direction) of the fibers.



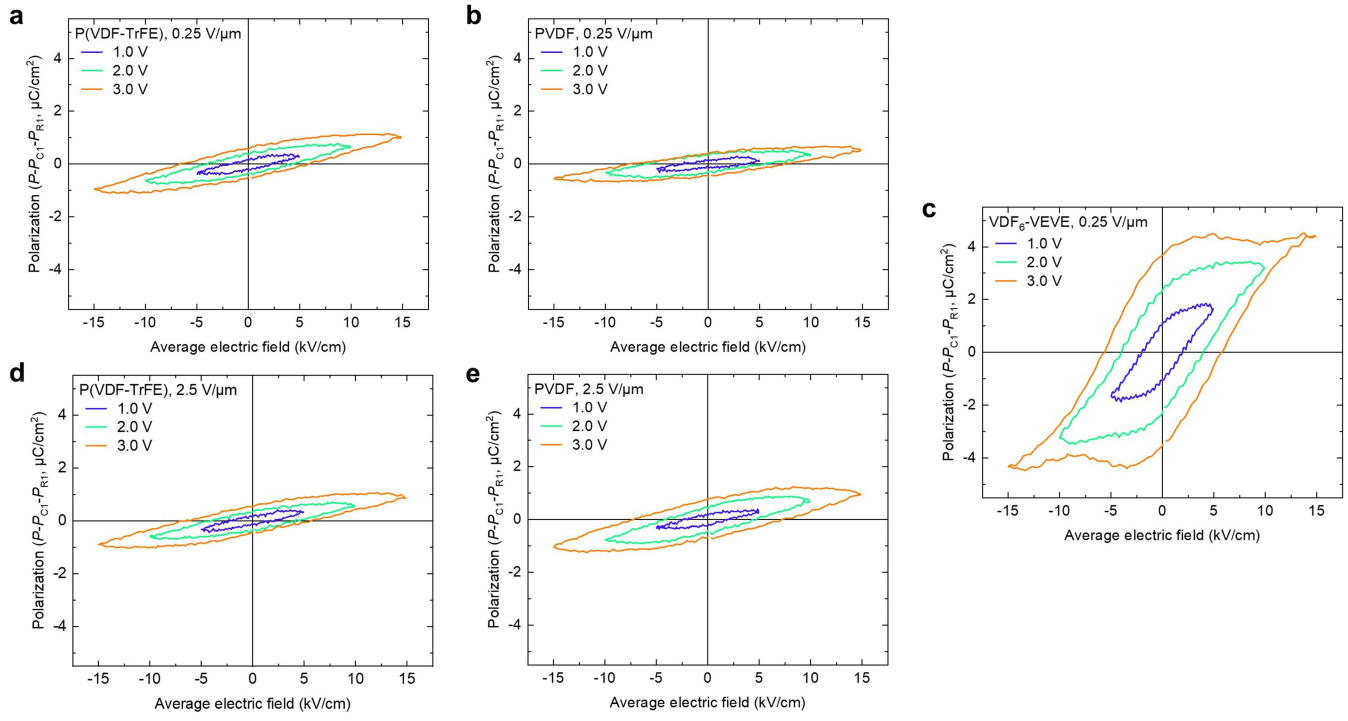
Extended Data Fig. 3 | AFM morphologies of the OVDF-PA and polymer films cast under an electric field. **a-b**, VDF₆-VEVE film prepared with an applied average electric field of 0.25 V/μm. **c-d**, PVDF and P(VDF-TrFE) (**e-f**) films prepared with an applied average electric field of 2.5 V/μm. White dashed lines indicate the 2 μm electrode gaps covered by the films; white arrows in (**b,d**, and **f**) indicate the direction of the applied electric field. The inset in (**d**) shows

the AFM height error map, which highlights the appearance of spherulites of PVDF and no obvious alignment of crystalline lamellae. **VDF₆-VEVE** fibers show preferential alignment along the direction of the applied electric field while typical crystal grain morphologies of P(VDF-TrFE) (**f**) show no obvious alignment.



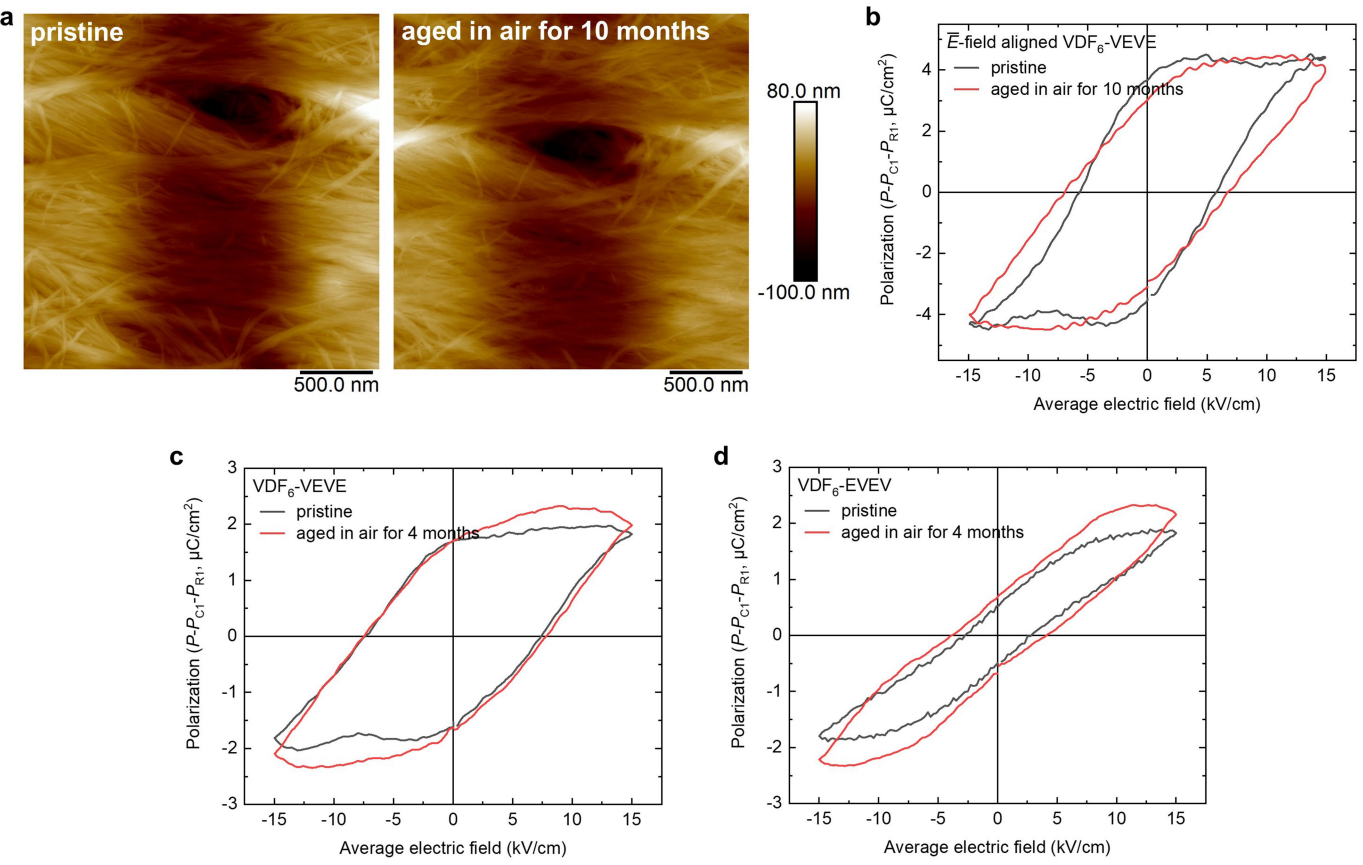
Extended Data Fig. 4 | Dielectric properties of the polymers and VDF₆-VEVE samples cast under electrical fields. **a-e**, Frequency domain capacitance and loss tangent of the P(VDF-TrFE) (**a**), PVDF (**b**), and VDF₆-VEVE (**c**) films cast under an average electric field of 0.25 V/ μ m and P(VDF-TrFE) (**d**) and PVDF (**e**)

films cast under an average electric field of 2.5 V/ μ m (see Methods) on the testing chip with a 2- μ m electrode gap measured at different amplitudes of AC voltages. **f**, Capacitance values measured at 0.5 V and 100 Hz were used as C₁ for data processing of the corresponding P-E loops.



Extended Data Fig. 5 | P-E loops of the polymers and VDF₆-VEVE samples cast under electrical fields. P(VDF-TrFE) (a), PVDF (b), and VDF₆-VEVE (c) films cast under an applied average electric field of 0.25 V/ μ m and P(VDF-TrFE) (d)

and PVDF (e) films cast under an average electric field of 2.5 V/ μ m (see Methods) with maximum applied voltages of 1.0 to 3.0 V.



Extended Data Fig. 6 | AFM morphologies and ferroelectric properties of the dried-state $\text{VDF}_6\text{-PA}$ assemblies aged at room temperature in air.
(a and b) Surface morphologies of the E -field aligned $\text{VDF}_6\text{-VEVE}$ assemblies before (left) and after (right) being aged at room temperature in air for

ten months. **(b)** P-E loops of the E -field aligned $\text{VDF}_6\text{-VEVE}$ sample before and after being aged at room temperature in air for ten months. **(c and d)** P-E loops of $\text{VDF}_6\text{-VEVE}$ (c) and $\text{VDF}_6\text{-EVEV}$ (d) samples after being aged at room temperature in air for four months in comparison with the pristine samples.